PAPER • OPEN ACCESS

Parametrization of a 0D solid oxide cell performance model—a detailed investigation including temperature dependencies of kinetic parameters

To cite this article: Marius Mueller *et al* 2025 *J. Phys. Energy* **7** 045006

Journal of Physics: Energy

PAPER

Parametrization of a 0D solid oxide cell performance model—a detailed investigation including temperature dependencies of kinetic parameters

Marius Mueller[1,2,*], **Markus Klinsmann**[1], **Ulrich Sauter**[1], **Jean-Claude Njodzefon**[1] and **André Weber**[2]

[1] Corporate Research, Robert Bosch GmbH, Renningen, Germany
[2] Institute for Applied Materials—Electrochemical Technologies (IAM-ET), Karlsruhe Institute of Technology (KIT), Karlsruhe, Germany
[*] Author to whom any correspondence should be addressed.

E-mail: marius.mueller5@de.bosch.com

Keywords: solid oxide cells, SOEC, electrolysis, kinetics, modeling, experimental parametrization, experimental validation

OPEN ACCESS

RECEIVED
25 March 2025

REVISED
17 June 2025

ACCEPTED FOR PUBLICATION
15 July 2025

PUBLISHED
29 July 2025

Abstract

The performance of a solid oxide cell (SOC) under given operating conditions is often predicted by using cell models that subtract the different voltage loss contributions from the theoretical Nernst voltage, also called open circuit voltage minus losses models. The determination of kinetic parameters for Butler–Volmer-type equations describing activation losses at fuel and air electrodes, respectively, is therefore originally conducted at a single operating temperature, resulting in temperature-independent values for these parameters. Yet, significant temperature gradients across both the cell area and the height of the stack occur in SOC applications; thus, a proper representation of the temperature dependency of all electrochemical parameters is required. We therefore examine possible temperature dependencies of the kinetic parameters and their impact on cell performance. To this end, the kinetic parameters are experimentally determined within the operating window of the investigated cell (600 °C–700 °C), showing nonnegligible temperature dependencies for all parameters of the Butler–Volmer-type equation. The impact of these temperature dependencies on cell performance is evaluated by comparing the error between measurements and simulations with and without temperature-dependent parameters. Accounting for temperature-dependent parameters reduces the maximum cell voltage error between simulation and measurement. This reduction was from −5.4% to −5.1% in the electrolysis mode and from −9.7% to −7.9% in the fuel cell mode when the parametrization temperature matched the operating temperature (compared to a 100 K offset). Although the cell voltage improvement was moderate, a significant impact was observed on activation overpotentials, where neglecting temperature dependence led to deviations of up to 56% for the investigated cell.

1. Introduction

A thorough understanding of the physical processes involved in a solid oxide cell (SOC) is mandatory for the effective development of this technology. These processes are interdependent, and to a great extent difficult or even unfeasible to approach by experimental means only. As such, suitable models have been developed to enable the study of experimentally inaccessible aspects of a cell under operation [1]. To ensure an accurate representation or prediction of the cell behavior, these models rely on appropriate physical assumptions and correct determination of the corresponding parameters.

Given the wide range of possible operating conditions of SOCs, such as temperature, flow rates, gas compositions, among others, numerous parameters need to be determined to achieve such an accurate representation of cell behavior. A possible approach to model the SOC behavior is computing the voltage losses associated with relevant processes and subtracting them from the Nernst voltage [1]. Often, the

respective calculations are performed using zero-dimensional equations that do not render the actual spatial extents of the cell or are considered only via cell dimension [1]. In all of these approaches, an adequate parametrization of the relevant voltage loss contributions is crucial. An approach to experimentally determine the cell-specific parameters of an equivalent circuit model (ECM) by fitting them to area-specific resistance data from electrochemical impedance spectroscopy (EIS) measurements is presented in [2]. The respective measurements were performed at various operating conditions relevant for fuel cell operations with H_2/H_2O as fuel, yielding a set of model parameters viable across all operating conditions. This approach is reproduced and varied in multiple subsequent works for CO/CO_2 operation [3], electrolysis mode [4], Ni/GDC fuel electrodes [5], and reformate operation [6]. A common assumption in earlier works dealing with Ni/YSZ fuel electrodes and LSCF air electrodes is a negligible temperature dependency of the Butler–Volmer parameters. However, given the complex nature of electrochemical reactions in SOCs, this assumption may not be fully justified. Later, for the material system of Ni/GDC, it was observed that the exponents accounting for the partial pressure dependence of the exchange current density are temperature-dependent, which is related to the pO_2 dependency of the conductivity of GDC [3, 5].

In this work, the parametrization of a cell model is performed at multiple temperatures using a commercially available fuel electrode–supported SOC [7]. A detailed analysis of the temperature dependencies of all model parameters is performed, and it is shown that the application of temperature-dependent parameters increases the model accuracy.

2. Method

In this work, a commercially available SOC manufactured by Elcogen [7] is investigated. The cell of type *ASC-300C* comprised a 273-μm-thick Ni/YSZ substrate, an 11-μm-thick Ni/YSZ fuel electrode functional layer, a 5 μm-thick YSZ electrolyte with 2-μm-thick GDC barrier layer, and a 26 μm-thick LSC air electrode, determined via scanning electron microscopy (SEM). The substrate dimensions are 5×5 cm^2 with an active area of 1.03 cm^2. The cell is heated up in safety gas (5% H_2 in N_2) and reduced at 700 °C in a heat-up routine recommended by Elcogen. The total flow rates during reduction and characterization are set to 0.605 nlm of fuel gas mixture and 1.283 nlm of O_2/N_2 gas mixture on the air side both flowing across the active width of the cell. Together with the small active area, this enables a minimal conversion of the duct gas and thus homogeneous conditions across the active cell area. The cell is operated under atmospheric pressure.

The procedure for determining the cell parameters is adopted from [2]. For this, impedance spectra are recorded within the frequency range 100 kHz–100 mHz using a *Zahner Zennium X* frequency response analyzer at systematically varied operating conditions of temperature (500°C–750°C), fuel side gas composition (between 0.05 atm and 0.9 atm for pH_2 and pH_2O), air side gas composition (0.02 atm–0.21 atm for pO_2), and current density (from open circuit voltage (OCV) to -1 A $\cdot$ cm^{-2} or 0.8 A$\cdot$cm^{-2} in electrolysis and fuel cell modes, respectively). Data quality and validity of the spectra are verified using Kramers–Kronig-Test (KKT) [8, 9], showing residuals mostly between $\pm$1% and no systematic deviation for all spectra (figure 1(a)).

An ECM is then fitted to the measured EIS data by complex nonlinear least squares minimization to determine and attribute the resistances of the occurring processes.

The distribution of relaxation times of the DRT of EIS measured at systematically varied operating conditions revealed that the ECM proposed in [2] comprised one resistor, three RQ elements, one Warburg element, and one Gerischer element connected in series, and can be used (figure 2). Here, the resistor represents the ohmic contributions (R_{ohm}), two RQ elements are assigned to the electrochemical processes of the fuel electrode (*resistive contribution denoted as* $R_{act,FE}$) and one RQ element to the gas diffusion in the air electrode ($R_{diff,AE}$). Gas diffusion in the fuel electrode ($R_{diff,FE}$) is represented by the Warburg element as the larger gas diffusion resistance (13–163 m$\Omega\cdot$cm^2) stands out more clearly in the impedance spectra and thus allows fitting a more complex element compared to a simple RQ element of the air electrode exhibiting gas diffusion resistance values of only up to 25 m$\Omega\cdot$cm^2. The Gerischer element is applied to describe the charge transfer and oxygen ion transport of the air electrode ($R_{act,AE}$). It is assumed that this ECM is transferable to the investigated cell, as both cells are fuel electrode–supported cells with the same layer materials, except for the air electrode material. The cell investigated in [2] comprises an LSCF air electrode, whereas the air electrode investigated in this work consists of an LSC. As both of these materials constitute single phases with mixed ionic and electronic conducting properties, they can be represented by a Gerischer element [10, 11].

Fitting the ECM to the 125 measured spectra leads to residuals not exceeding $\pm$1% except for single outliers, as shown in figure 1(b). Once again, this demonstrates the suitability of the chosen ECM [5] in determining the exponents of the partial pressure dependencies of the exchange current density for a Ni/GDC fuel electrode at six temperatures in the range of 600 °C–900°C for which values valid for specific

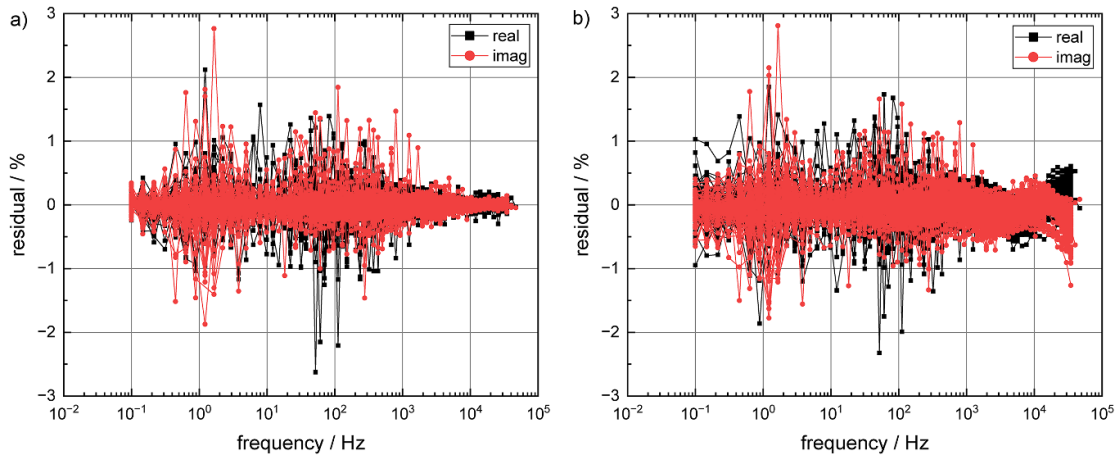

Figure 1. (a) Kramers–Kronig test residuals and (b) equivalent circuit model fit residuals as a function of frequency for all 125 evaluated spectra.

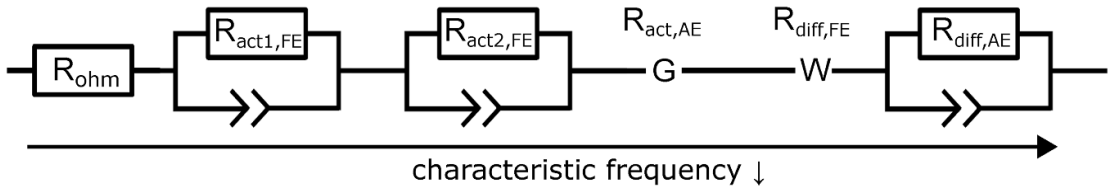

Figure 2. Employed equivalent circuit model for the investigated cell.

temperature ranges or expressions for temperature dependency were deduced. This becomes necessary for Ni/GDC electrodes where both charge transfer and ionic conduction in the ceria phase depend differently on temperature and gas composition. In the case of Ni/YSZ, the ionic conductivity depends solely on temperature, thus allowing for a simpler modeling. For both cases, a physically more appropriate modeling approach would be a transmission line model, for which parameterization requires a more detailed knowledge of the microstructural and electrical properties of the electrode layer [12, 13].

Electrochemical reactions at the electrodes involve multiple steps [14], with varying rate-determining steps at different temperatures. Therefore, investigating the temperature dependency of partial pressure dependencies and charge transfer effects is warranted.

In previous works on Ni/YSZ fuel electrodes [2, 4], component gas partial pressure and current density were varied at one temperature (800 °C). In this work, these variations are conducted at three temperatures 600 °C, 650 °C, and 700 °C. Each ECM fit yielded values for the six resistances attributed to the different processes in the cell. The resistance values were then further processed by fitting adequate equations to deduce their dependency on the corresponding operating conditions.

To perform the analysis of the impedance spectra, including KKT, DRT, and ECM fitting, the open-source python package *deareis* [15] was used.

In order to derive temperature and gas composition dependencies, EIS measurements were conducted at OCV, whereas EIS measurements for the charge transfer coefficients α were performed under load.

The determination of the microstructural and electrochemical parameters is based on two consecutive fitting steps. First, the ECM is fitted to the measurement data to yield resistances ascribed to the individual processes in the cell. Nonlinear equations are fitted to these resistances to derive their dependencies on operating conditions, yielding physically interpretable model parameters. By default, this approach involves assumptions and introduces potential error sources. This should be kept in mind while analyzing the fitting results and also while employing the deduced parameters in the 0D model.

In the following the subscript AE, FE, and el are used to denote air electrode, fuel electrode and either electrode, respectively.

3. Parametrization

3.1. Microstructure

Gas diffusion polarization occurs when reactants are transported to, and products away, from reaction sites, respectively. The gas diffusion resistance generally becomes rate limiting at high current densities when a sufficient supply of reactants to the reactive sites can no longer be maintained. The magnitude of this resistance is significantly influenced by the microstructure of the porous electrodes. The properties of porous microstructures are commonly described by the porosity ε, that is, the void volume fraction ranging from 0 to 1, and the tortuosity τ—a measure of the effective relative diffusion path length with a lower bound of 1 for completely undistorted paths. In the model, both parameters are included in a quotient—the microstructural parameter Ψ, defined as the ratio of porosity to tortuosity $\left(\Psi = \frac{\varepsilon}{\tau^2}\right)$. In this work, a microstructural parameter Ψ_{el} per electrode *el* is determined, which is the resulting quantity representing the combined microstructural properties of multiple layers. Ψ_{el} was determined by varying binary gas mixtures at each electrode. At the fuel electrode, the H_2/H_2O ratio was varied between 10/90 and 90/10, whereas air is supplied to the air electrode minimizing its gas diffusion resistance. For the air electrode, the O_2/N_2 ratio was varied between 2/98 and 10/90. To shift the fuel side gas diffusion process to higher frequencies and ease the separation of the gas diffusion processes of both electrodes occurring at low frequencies, the fuel side gas composition was set to $H_2/H_2O = 50/50$. Fitting of Ψ_{el} is performed with equation (1) [16, 17] for the fuel electrode and equation (2) [16, 17] for the air electrode. From these equations, $R_{diff,el}$ is determined from the CNLS fit of the low frequency peak of each electrode (fitted to a Warburg element for the fuel electrode and an RQ element for the air electrode) and the thickness of the respective electrode L_{el} from SEM analysis. The molar diffusion coefficients $D_{mol,i}$ are determined via the Bosanquet equation (equation (3)) [18] and the results from both the bulk $D_{bulk,i}$ (via Chapman–Enskog (4) [16, 19] and Wilke (5) [20] approach) and Knudsen $D_{kn,i}$ [19, 21] diffusion coefficients of a species *i*. For the calculation of the latter, a value for the mean pore radius $r_{pore,el}$ is required, see equation (6). In these equations, R denotes the ideal gas constant, F the Faraday constant, T the absolute temperature, p the total pressure, p_i the partial pressure of species *i*, M_i and M_j are the molar mass and x_i and x_j are the molar fraction of species *i* and *j*, respectively. σ_{ij} is their average collision diameter, and Ω_{ij} is the collision integral. Average collision diameter and collision integral were calculated using data by [22] provided in [19]. Due to the lack of own measurements, the values of $r_{pore,FE} = 410$ nm and $r_{pore,AE} = 261$ nm are assumed [23] as they result from a comprehensive and well-documented experimental microstructural study for a fuel electrode–supported cell with the same fuel electrode and a similar air electrode chemistry [24]. As explained above, Ψ_{el} is obtained by fitting $R_{diff,el}$ with equations (1) and (2) with given diffusion coefficients, which are influenced by $r_{pore,el}$. Therefore, Ψ_{el} is adjusted to best represent the determined $R_{diff,el}$ for the assumed $r_{pore,el}$. If $r_{pore,el}$ is overestimated, $D_{Kn,i}$ is also overestimated (equation (6)) and $D_{mol,i}$ (equation (3)), resulting in an underestimation of Ψ_{el} to reach the same $R_{diff,el}$ (equations (1) and (2)). With the same reasoning, an underestimation of $r_{pore,el}$ leads to an overestimation of Ψ_{el}. Although imprecise values of the mean pore radii may impair the model accuracy, the error is minimal as long as Ψ_{el} is consistent with the assumed $r_{pore,el}$:

$$R_{\mathrm{diff,\,FE}} = \left(\frac{RT}{2F}\right)^2 L_{\mathrm{FE}} \frac{1}{\psi_{\mathrm{FE}}} \left(\frac{1}{D_{\mathrm{mol,\,H_2}} \cdot p\mathrm{H_2}} + \frac{1}{D_{\mathrm{mol,\,H_2O}} \cdot p\mathrm{H_2O}}\right) \cdot \left(1.0133 \cdot 10^5 \frac{\mathrm{Pa}}{\mathrm{atm}}\right)^{-1} \tag{1}$$

$$R_{\mathrm{diff,\,AE}} = \left(\frac{RT}{4F}\right)^2 L_{\mathrm{AE}} \frac{1}{D_{\mathrm{mol,\,O_2}}} \frac{1}{\psi_{\mathrm{AE}}} \left(\frac{1}{p\mathrm{O_2}} - 1\right) \cdot \left(1.0133 \cdot 10^5 \frac{\mathrm{Pa}}{\mathrm{atm}}\right)^{-1} \tag{2}$$

$$\frac{1}{D_{mol,i}} = \frac{1}{D_{bulk,i}} + \frac{1}{D_{kn,i}} \tag{3}$$

$$D_{bulk,ij} = \frac{1.86 \cdot 10^{-3} \cdot T^{1.5} \sqrt{M_i^{-1} + M_j^{-1}}}{p \cdot \sigma_{ij}^2 \cdot \Omega_{ij}} \tag{4}$$

$$D_{bulk,i} = \frac{1 - x_i}{\sum_{j \neq i} \left(x_j / D_{bulk,ij}\right)} \tag{5}$$

$$D_{kn,i} = \frac{2}{3} r_{pore,el} \sqrt{\frac{8}{\pi} \cdot \frac{RT}{M_i}}. \tag{6}$$

Since the microstructure is independent of temperature, a determination of Ψ_{el} at one operating temperature is sufficient. Therefore, it is favorable to select the highest investigated temperature of 700 °C as

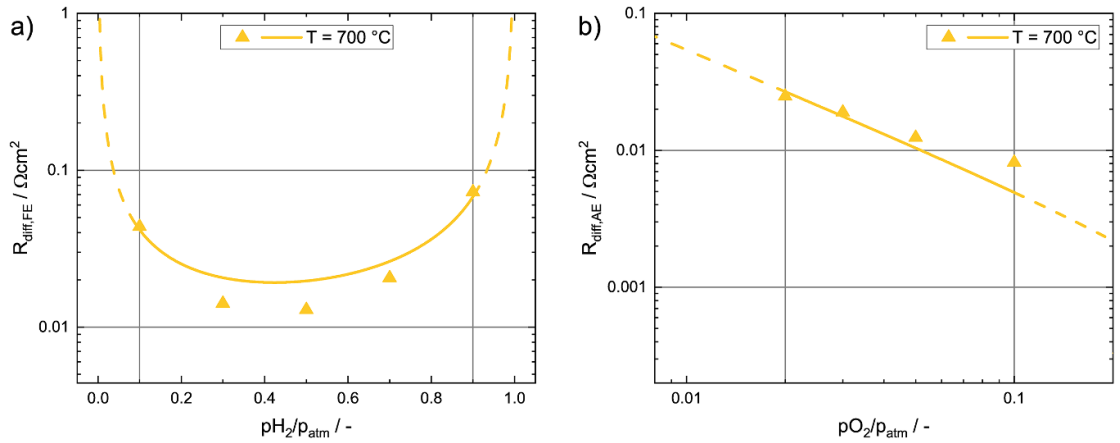

Figure 3. Gas diffusion resistances $R_{diff,el}$ in the dependency of the binary gas composition at 700 °C for (a) the fuel electrode and (b) the air electrode. Values of $R_{diff,el}$ determined by ECM fits are shown as symbols, the fits of the fuel electrode by equation (1) and of the air electrode by equation (2) as lines and their respective extrapolations by dashed lines. A total fuel gas flow rate $\dot{V}_{fuel} = 0.605$ nlm and total air flow rate $\dot{V}_{oxidant} = 1.283$ nlm is set with $p_{atm} = 1$ atm and $A_{active} = 1.03$ cm^2. In (a), air is set at the air electrode and in (b) a fuel gas composition of $H_2/H_2O = 50/50$ is set at the fuel electrode.

the separation in the frequency domain between the gas diffusion processes and thermally activated electrochemical processes increases with temperature.

Determining Ψ_{FE} at 700 °C by fitting equation (1) to the determined $R_{diff,FE}$, as shown in figure 3(a) leads to a value of 0.037. This value is 72% smaller than the one determined by [2] ($\Psi_{FE} = 0.13$), suggesting either a smaller volume fraction of the gas phase and/or higher tortuosity on the substrate of the investigated cell. This implies increased gas transport resistance and, potentially, a higher solid phase fraction (Ni, YSZ, or both) within the fuel electrode, leading to an improved charge transport. Microstructural analysis presented in the literature supports this assumption as a gas volume fraction of 0.415 [23, 24] was found for the cell investigated in [2], whereas 0.36 [25] was determined for the cell examined in this work.

In addition to transport resistances, the fuel electrode substrate in this type of cell provides mechanical stability for the cell. The thickness of the substrate of the investigated cell is only 27.5% of that of the one investigated in [2]; therefore, a sufficient amount of the solid phase is needed to ensure mechanical robustness. A linkage between substrate thickness and phase fraction is also observed in the quotient $L_{substrate}/\Psi_{FE}$, which enters equation (1) as the main cell-specific prefactor determining the gas diffusion resistance. For this quotient, similar values were found in this work (0.0071 m) and in [2] (0.0077 m). With the assumption of the same $r_{pore,FE}$ for both cells and at the same operating conditions, this leads to a 7.3% lower $R_{diff,FE}$ for the investigated cell.

For the equivalent parameter of the air electrode Ψ_{AE}, the application of equation (2) yields a value of 0.028 (figure 3(b)). The Ψ_{AE} determined for this cell is about 69% smaller than the one presented in [2], indicating a higher solid phase fraction on the air side too.

3.2. Ohmic losses

In SOCs, the ohmic resistance includes the resistance of electrons and oxygen ions through all layers of the cell. The model is fitted for different temperatures using an Arrhenius-type equation, see equation (7). Commonly, the activation energy $E_{act,ohm}$ reflects the energy barrier a charge carrier has to overcome in order to move through the material. Its impact on the resulting ohmic resistance is highest for low temperatures and decreases with increasing temperature. The proportionality constant B_{ohm} depends on the material and structural properties. It represents an inverse measure for the frequency of attempts to cross the barrier. The impact on the resulting ohmic resistance is linear and independent of temperature and also includes the resistance resulting from the contacting of the cell in the measurement setup. The ohmic resistance increases with larger values of $E_{act,ohm}$ and smaller values of B_{ohm}:

$$R_{ohm}(T) = \frac{T}{B_{ohm}} \cdot e^{\left(\frac{E_{act,ohm}}{RT}\right)}. \tag{7}$$

In our approach, only a single equation and related apparent activation energy is used to describe all ohmic contributions to the cell resistance. Therefore, equation (7) should be understood as an empirical approach with coefficients that result from a combination of materials and microstructures of the different layers in the cell.

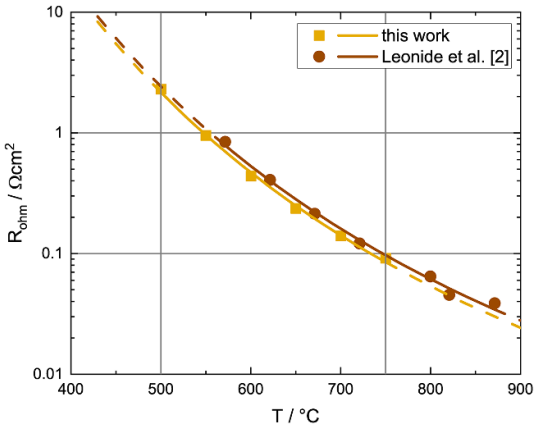

Figure 4. Ohmic resistance R_{ohm} as a function of temperature for the investigated cell and the one reported in [2]. Values determined by ECM fits are shown as symbols. Fits using equation (7) are shown as solid interpolation lines within the measured temperature range and as dashed extrapolation lines for temperatures outside the measured range. For the investigated cell a fuel gas composition of $H_2/H_2O = 50/50$ and air with a total fuel gas flow rate $\dot{V}_{fuel} = 0.605$ nlm and total air flow rate $\dot{V}_{oxidant} = 1.283$ nlm is set with $p_{atm} = 1$ atm and $A_{active} = 1.03$ cm^2.

The ohmic resistance is assumed to be independent of gas composition, which was confirmed experimentally by the conducted variations of pO_2 and pH_2/pH_2O at different temperatures. On the fuel side, this assumption is valid as the conductivity of neither YSZ nor Ni shows a distinct pO_2 dependency. For the air side, this is a simplification, as the GDC barrier layer and air electrode material (LSC) display a small but measurable increase in conductivity with decreasing pO_2 [26, 27]. The overall contribution to the ohmic resistance is believed to be small for these two layers and the fuel electrode as the resistance is dominated by the YSZ electrolyte and the YSZ–GDC interdiffusion layer [28, 29]. Therefore, no additional parameter considering the pO_2 dependency of the ohmic resistance is included, and the coefficients of equation (7) are attributed to the combination of the YSZ electrolyte and YSZ–GDC interdiffusion layer.

The ohmic resistance of the investigated cell is determined for a temperature range of 500°C–750 °C (figure 4). The gas composition is set to $H_2/H_2O = 50/50$ on the fuel side and air ($O_2/N_2 = 21/79$) on the air side.

While fitting the determined R_{ohm} to equation (7), significant deviations of the resulting parameters B_{ohm} and $E_{act,ohm}$ are observed depending on the weighting method applied. Logarithmic weighting is applied here due to the order-of-magnitude variation in R_{ohm} across the investigated temperature range. To ensure a consistent comparison, the values of R_{ohm} from [2] were fitted again using the same method as for the data in this work. This resulted in B_{ohm} and $E_{act,ohm}$ values that are 25.8% and 1.9% higher, respectively, than those reported in [2].

The fitting procedure yields an activation energy $E_{act,ohm}$ of the investigated cell that is only 0.6% higher $E_{act,ohm}$ (92.56 kJ·mol^{-1}) compared to [2]. This negligible difference is a result of identical material selection in both cells for the components that dominate the ohmic resistance, that is, for electrolytes, barriers and interdiffusion layers. Slight differences in $E_{act,ohm}$ for both cells are expected; nonetheless, as their value is also influenced by several cell manufacturing properties, for example, purity of raw materials, powder properties, and sinter temperatures.

Compared to B_{ohm}, a 21.6% higher value ($6.41 \cdot 10^{12}$ S·K·m^{-2}) for the investigated cell as compared to [2] is found, leading to a lower R_{ohm} for the investigated cell at the same operating temperature as shown in figure 4.

3.3. Activation losses

The charge transfer reaction occurs in the vicinity of the triple or double phase boundaries of the respective electrodes. A commonly applied approach to describe the dependence of the current density j on the activation overpotential η_{act} at these sites is the so-called Butler–Volmer equation (equation (8)):

$$j = j_+ - j_- = j_{0,el}\left(e^{\left(\alpha_{el}\frac{n_e F \eta_{act,el}}{RT}\right)} - e^{\left(-(1-\alpha_{el})\frac{n_e F \eta_{act,el}}{RT}\right)}\right). \quad (8)$$

where η_{act} denotes the activation overpotential, α is the so-called charge transfer coefficient, $n_e = 2$ refers to the number of electrons exchanged, and j_0 is the exchange current density. Expanding the bracket gives two terms proportional to j_0 that describe the rate of reaction in the forward (j_+) and backward (j_-) directions of

the reaction. Hence, j_0 is a measure of the reactiveness of the electrode. At zero overpotential, that is under the absence of an external load, the reaction rates in both directions cancel each other out resulting in a net zero current density.

The usage of the Butler–Volmer equation in the field of SOCs is often discussed controversially [30] since central conditions assumed [31], such as the limitation to single-step reactions, are generally not fulfilled [30, 32]. Instead, the reactions at the electrodes of an SOC involve a chain of multiple coupled steps with ionic, electronic, and gas phase transport [33]. However, the application of the equation as an empirical relation [34] is nonetheless widespread due to its good agreement with experimental data over a broad range of currents and operating conditions [2, 4].

Various variants of the equation can be found in the literature. The version given in equation (8) and used throughout this work compromises a condition on the exponents of the forward and backward reaction terms, namely that the charge transfer coefficients sum to one ($\alpha + (1 - \alpha) = 1$). Under this condition, the charge transfer coefficients describe the ratio of forward and backward reaction rates [31]. A benefit of this assumption is a direct relation between the exchange current density j_0 and the activation resistance at OCV conditions R_{act}, given by:

$$j_{0,\mathrm{el}} = \frac{1}{R_{\mathrm{act,el}}} \cdot \frac{RT}{2F} \tag{9}$$

that is found by the linearization of equation (8) around $\eta_{\mathrm{act}} = 0$ and usage of $R_{\mathrm{act,el}} = \partial_j \eta_{\mathrm{act}}$. Hence, in this approach, the exchange current density can be obtained directly from the activation resistance at OCV conditions independently of any other parameters and does not require additional fitting steps.

To differentiate between activation losses stemming from the air and fuel electrode, separate Butler–Volmer-type equations are adopted for each electrode, respectively. Activation overpotentials and current densities in equation (8) are thereby replaced by their electrode-wise counterparts j_{AE}, j_{FE} and $\eta_{\mathrm{act,AE}}$, $\eta_{\mathrm{act,FE}}$, respectively, and both charge transfer coefficients and exchange current densities become electrode-specific, that is, α_{AE}, α_{FE} and $j_{0,\mathrm{AE}}$, $j_{0,\mathrm{FE}}$ [2]. An extension of this approach also distinguishing between the operating modes, by allowing separate parameters for fuel cell and electrolysis operations, is discussed further below.

The exchange current densities entering the electrode-wise Butler–Volmer equations are not a fixed value but instead depend on the local conditions, that is, gas composition and temperature. Commonly used assumptions for these dependencies are given by:

$$j_{0,\,\mathrm{AE}} = \gamma_{\mathrm{AE}} \left(\frac{p\mathrm{O}_2}{p_{\mathrm{atm}}} \right)^m \cdot \mathrm{e}^{\left(-\frac{E_{\mathrm{act,\,AE}}}{RT} \right)} \tag{10}$$

$$j_{0,\,\mathrm{FE}} = \gamma_{\mathrm{FE}} \left(\frac{p\mathrm{H}_2}{p_{\mathrm{atm}}} \right)^a \cdot \left(\frac{p\mathrm{H}_2\mathrm{O}}{p_{\mathrm{atm}}} \right)^b \cdot \mathrm{e}^{\left(-\frac{E_{\mathrm{act,\,FE}}}{RT} \right)}. \tag{11}$$

In the following section, we first examine the partial pressure dependencies expressed by the exponents *a*, *b*, and *m*, then extract the activation energies $E_{\mathrm{act,AE}}$ and $E_{\mathrm{act,FE}}$, as well as the proportionality factors γ_{AE} and γ_{FE} and finally determine the electrode- and potentially operating mode-wise charge transfer coefficients introduced by equation (8).

3.3.1. Partial pressure dependency

In [2], the exponents *a, b,* and *m* were determined at a single temperature of 800 °C and assumed to be temperature-independent as to be expected considering the physicochemical background of the BV-equation. This approach provides a good agreement with experimental results for a temperature range from 621°C to 821°C.

In [5], investigating a Ni/GDC fuel electrode over a wide temperature range from 600 °C to 900°C, a temperature dependency of the parameters *a* and *b* was observed, with a linear expression found for parameter *b* for the investigated temperature range. For parameter *a*, two values were obtained, one for the temperature range of 600 °C–750°C and the other for 800 °C–900°C.

In this study, the lower operating temperature of the investigated cell did not call for investigations well above 700 °C. Therefore, the exponents *a* and *b* for the dependency of $j_{0,\mathrm{FE}}$ on $p\mathrm{H}_2$ and $p\mathrm{H}_2\mathrm{O}$ (equation (11)) and the exponent *m* for the dependency of $j_{0,\mathrm{AE}}$ on $p\mathrm{O}_2$ (equation (10)) are determined at fixed operating temperatures of 600 °C, 650 °C, and 700 °C under OCV conditions by varying the fraction of the respective gas components. This is conducted by balancing the gas mixture with $p\mathrm{N}_2$.

Table 1 presents the operating conditions chosen in this work.

Table 1. Operating conditions at OCV for the determination of the partial pressure dependencies *a*, *b*, and *m*.

		Fuel side			Air side	
Parameter	T (°C)	pH_2 (atm)	pH_2O (atm)	pN_2 (atm)	pO_2 (atm)	pN_2 (atm)
a	600, 650, 700	0.6, 0.4, 0.2, 0.1, 0.05	0.4	0.0, 0.2, 0.4, 0.5, 0.55	0.21 (air)	0.79 (air)
b	600, 650, 700	0.6	0.4, 0.3, 0.2, 0.1, 0.05	0.0, 0.1, 0.2, 0.3, 0.35	0.21 (air)	0.79 (air)
m	600, 650, 700	0.5	0.5	0.0	0.21, 0.1, 0.05, 0.03, 0.02	0.79, 0.9, 0.95, 0.97, 0.98

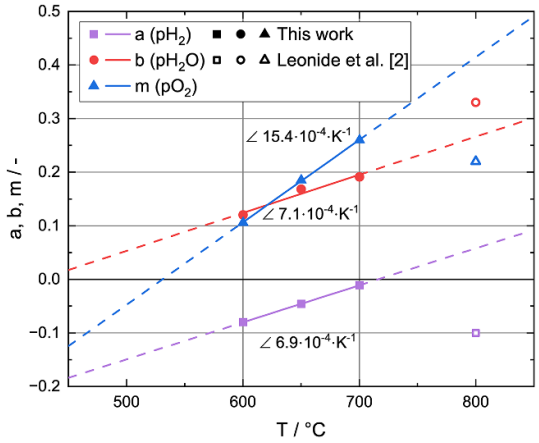

Figure 5. Determined partial pressure dependencies *a*, *b*, and *m* of the exchange current density as a function of temperature. Values determined via gas composition variation are shown as symbols at their respective temperature for the investigated cell (full, between 600 °C and 700 °C) and the one investigated in [2] (empty, at 800 °C). Linear fits for the temperature dependency of the here investigated cell are shown as solid interpolation lines within the measured temperature range and as dashed extrapolation lines for temperatures outside the measured range.

The coefficients *a, b*, and *m*, expressing the dependency of $j_{0,el}$ on the partial pressures of the respective reactants (see equations (10) and (11)), are determined as the negative values of the slope of the activation resistance $R_{act,el}$ (equation (9)) against the partial pressures using a double logarithmic scale [2].

The parameter value of zero corresponds to a vanishing influence of the respective partial pressure on the activation resistance. A positive value reflects a decreasing resistance due to an increase in the partial pressure of the component. For the investigated cell, this is the case for H_2O (*b*) and O_2 (*m*), as shown in figure 5. The value *a* for H_2 is found to be negative for the cell under investigation (figure 5), meaning that the resistance increases with increasing pH_2.

Using equations (10) and (11), it can be derived that the relative slope of the exchange current density with respect to the partial pressure of a component *i* is $\partial_{p_i} j_0 / j_0 = x/p_i$, where $x = a$, *b*, or *m* is the exponent of component *i*. Hence, the sensitivity of the exchange current density (and activation resistance as linked via equation (9)), on the changes in the partial pressure of a component relative to its current value is directly proportional to the magnitude of the respective exponent (appendix 1).

To study the influence of temperature on *a, b*, and *m*, their determination is performed at multiple temperatures. All three parameters display a significant change with temperature in the investigated range of 600 °C–700 °C, ranging from −86.3% for *a* to +59.2% for *b* and +145.2% for *m*. The increase of *b* and *m* with increasing temperature shows that the dependency of the activation resistance on pH_2O and pO_2 increases for higher temperatures, whereas it decreases for pH_2, as *a* tends toward 0. This has implications for the operation of larger systems as the optimization of gas composition with respect to low cell resistance will differ depending on the local temperature. Thus, different values for gas conversion and/or the recirculation of gas stream flow might prove to be advantageous.

Approximating the temperature dependency of the parameters with a linear function over the investigated temperature range (figure 5) yields good fits with R^2 values of 0.96 and higher. The slopes for all three parameters are positive with the exponents of pH_2 (a) and pH_2O (b) showing similar values of $6.9 \cdot 10^{-4}$ K^{-1} and $7.1 \cdot 10^{-4}$ K^{-1}, respectively. However, since the value of a is negative in the temperature range investigated, it tends toward smaller absolute values for higher temperatures, whereas the magnitude of b increases. It is apparent that the slope of the exponent for pO_2 (m) with $15.4 \cdot 10^{-4}$ K^{-1} is about twice as steep as the slopes for a and b. Thus, the pO_2 dependency of the activation resistance at the air electrode is more sensitive to temperature change than the pH_2 and pH_2O dependency of the activation resistance at the fuel electrode.

Extrapolating the linear fits to higher temperatures, one finds that a changes from negative to positive values at around 716°C (989 K). This would mean that at even higher temperatures, an increase in the hydrogen partial pressure results in a decrease in activation resistance or increase in the exchange current density. From a kinetic point of view, this turnaround suggests a change in the rate determining step of the reaction mechanism for the investigated cell while crossing the described zero-crossing temperature. It means that, due to the different activation energies of individual reaction steps [14, 35], increasing temperature shifts the rate-limiting step to one favoring operation with higher pH_2. As the exponent of the steam partial pressure b is also positive in this temperature regime, increasing the partial pressure of both components would reduce the activation resistances, favoring the reaction rate. This can be achieved through pressurized operation; in that case, a part of the required energy for gas compression can be offset by an improved kinetic and therefore reduced activation overpotentials. However, while operating SOCs above atmospheric pressure influences on other parameters of functionality, such as the Nernst voltage, have to be considered while assessing the impact of the partial pressure dependencies on cell performance [36, 37].

An alternative trend of a toward higher temperatures that could also be plausible, instead of the linear extrapolation, is the convergence to a value of 0. In this scenario, and with the exception of the limiting case in which a is 0, the activation resistance would still increase with increasing values of hydrogen partial pressure pH_2, for example, at high steam conversion rates in the electrolysis mode. However, the increase in the resistance with increasing pH_2 would become less steep.

With the exception of the value of m at 700 °C, the absolute values of the exponents determined in this work are generally smaller than the ones obtained by [2] at 800 °C. This implies that the sensitivity of the exchange current density to the gas composition is less pronounced for the cell and temperature range investigated in this work.

Using the suggested linear fits to extrapolate to an operation temperature of 800 °C at which the authors in [2] parametrized their cell, significant differences in the parameter values can be observed. Parameter a would have a positive value (0.058) for the cell investigated in this work, compared to a negative value (−0.10) determined by [2]. As mentioned earlier, this would indicate a change in the rate determining step of the reaction mechanism of the fuel electrode, where the reaction rate at the fuel electrode, although with about half as much dependency (0.058 vs. 0.1), *increases* with increasing pH_2. The extrapolated value for the H_2O partial pressure dependency b (0.266), though smaller, is much more comparable to that determined by [2] (0.33) with a deviation of only −19.3%. In contrast, the extrapolated value of m (0.415) is 88.5% larger compared to the 0.22 in [2]. These values suggest that, with all other parameters being equal, and for a given $pO_2 < 1$ atm, the oxygen electrode of the cell in [2] would have a higher exchange current density versus the cell investigated here.

The temperature dependencies demonstrated in this work for parameters a, b and m suggest that the reaction kinetics at the fuel and air electrodes of the SOC have different degrees of dominance and/or rate limiting steps at different temperatures in and for the investigated temperature range and SOC chemistries, respectively. These findings experimentally enhance the idea that the SOC kinetics is not governed by pure Butler–Volmer kinetics [30]. However, as will be demonstrated further below, a *Butler–Volmer-type* equation can most definitely be employed to describe the SOC kinetics at both electrodes while simulating activation losses at these electrodes [2, 4].

The distinct temperature dependency of a, b, and m implies that using the same set of parameters for a wide range of temperatures can lead to nonnegligible deviations between predicted and actual cell performance, particularly in the presence of temperature gradients within the cell.

3.3.2. Activation energy

In addition to the partial pressure of reactant gases, the exchange current density also depends on the operating temperature. This influence is predominantly considered via an Arrhenius-type approach with a respective activation energy $E_{act,el}$ and a temperature-independent proportionality constant B_{el} for each electrode (equation (12)).

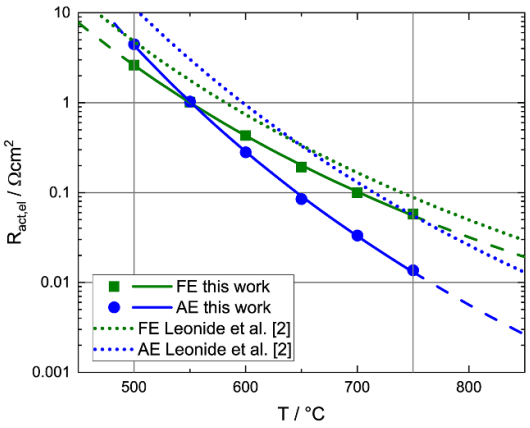

Figure 6. Activation resistance $R_{act,el}$ for fuel and air electrodes as a function of temperature T. The resulting values of the fit presented in [2] are shown as dotted lines. Values determined for the investigated cell in the temperature range between 500°C and 750°C are shown as symbols. Fits using equation (12) are shown as solid interpolation lines within the measured temperature range and as dashed extrapolation lines for temperatures outside the measured range. For the investigated cell, a fuel gas composition of $H_2/H_2O = 50/50$ and air with a total fuel gas flow rate $\dot{V}_{fuel} = 0.605$ nlm and total air flow rate $\dot{V}_{oxidant} = 1.283$ nlm is set with $p_{atm} = 1$ atm and $A_{active} = 1.03$ cm^2.

The apparent activation energies are determined through a temperature variation in OCV, for which the activation resistances $R_{act,el}$ are extracted via CNLS fits of the recorded spectra. Here, the temperature is varied in 50 K steps between 500°C and 750°C, whereas a gas composition of $H_2/H_2O = 50/50$ on the fuel side, and air ($O_2/N_2 = 21/79$) on the air side is set.

The applied Arrhenius-type function yields excellent fit qualities ($R^2 = 1$) for both electrodes, as seen in figure 6:

$$R_{act,\,el}\,(T) = B_{el} \cdot e^{\left(\frac{E_{act,\,el}}{RT}\right)}. \tag{12}$$

For a set of gas compositions, the air electrode displays an apparent activation energy of 152.8 kJ mol^{-1} (1.58 eV)—a 50.7% higher activation energy than the fuel electrode, with 101.4 kJ mol^{-1} (1.05 eV), leading to a higher activation resistance of the air electrode for temperatures below 550°C. For temperatures above 550°C, the ratio of the resistances is inverted as the substantially smaller value of B_{AE} ($2.06 \cdot 10^{-14}$ S^{-1}·m^2) compared to B_{FE} ($3.70 \cdot 10^{-11}$ S^{-1}·m^2) commands an overall lower activation resistance. The combination of a significantly larger $E_{act,AE}$ and smaller B_{AE} results in a significantly more pronounced temperature dependency of the activation resistance for the air electrode. In [2], the same relation between fuel and air electrode is found, but with less pronounced differences between the values of $E_{act,el}$ and B_{el} for both electrodes.

For the fuel electrode only minor differences between both cells are found. B_{FE} of the cell investigated in this work is 3.4% smaller and $E_{act,FE}$ is 3.5% smaller compared to [2], resulting in a lower activation resistance. Small differences are expected due to the same material and different microstructures.

For the air electrode, the differences in the determined parameter values are more significant with B_{AE} being 94.9% smaller and $E_{act,AE}$ 9.3% larger for the investigated cell. This results in smaller activation resistances in the relevant temperature range (above 250°C). The large differences between the two cells are attributed to the differing electrode materials (LSC vs. LSCF in [2]). The B_{AE} values suggest a much better electrode microstructure for the LSC electrode compared to the LSCF electrode. Since both are single phase MIEC materials, the 9.3% difference in activation energies may not be large enough to suggest a major difference in reaction mechanism, but rather indicate that one or more reaction steps are slightly more challenged in the air electrode of the cell investigated in this work.

3.3.3. Proportionality factor γ

To fully define the exchange current density $j_{0,el}$ (equations (10) and (11)) the Butler–Volmer-type equation (8), the proportionality factor γ_{el} must be determined. This is done by evaluating the equations (13) and (14) for the three investigated temperatures, where B_{FE} and B_{AE}, as well as the temperature-dependent *a, b*, and *m*, are taken from the above described evaluations:

$$\gamma_{FE}\left(\frac{pH_2}{p_{atm}}\right)^a\left(\frac{pH_2O}{p_{atm}}\right)^b = \frac{RT}{2FB_{FE}} \tag{13}$$

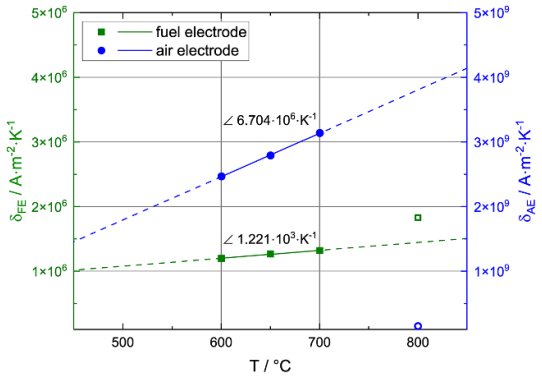

Figure 7. Prefactor δ_{el} of the proportionality factor γ_{el} for fuel and air electrodes as a function of temperature. Values determined by experimental data are shown as symbols at their respective temperature for the investigated cell (full) and the one investigated in [2] (empty). Linear fits for the temperature dependency of the investigated cell are included as solid interpolation within the measured temperature range and as dashed extrapolation lines for temperatures outside the measured range.

Table 2. Current densities at which EIS measurements for the determination of the charge transfer coefficients α were conducted at the investigated temperatures. Absolute current densities investigated for both operation modes are shown in the second column, current densities solely investigated in electrolysis (EC) or fuel cell (FC) mode are shown in the third resp. fourth column.

T (°C)	EC and FC mode $\lvert j\rvert$ (A·cm^{-2})	Only EC mode j (A·cm^{-2})	Only FC mode j (A·cm^{-2})
600	0.0, 0.025, 0.05, 0.075, 0.1, 0.15, 0.2	—	0.25, 0.3
650	0.0, 0.025, 0.05, 0.075, 0.1, 0.15, 0.2, 0.25, 0.3, 0.4, 0.5	−0.55	0.6
700	0.0, 0.05, 0.1, 0.15, 0.2, 0.3, 0.4, 0.6, 0.8	−1.0	—

$$\gamma_{AE}\left(\frac{pO_2}{p_{atm}}\right)^m = \frac{RT}{2FB_{AE}}. \tag{14}$$

The proportionality factor γ_{el} is considered as a temperature-independent prefactor δ_{el} multiplied with the absolute temperature, see equation (15) [2]. However, it is found that for both electrodes, the value of δ_{el} increases with temperature. The results are shown in figure 7. For the investigated temperature range from 600 °C to 700 °C, δ_{FE} grows by about 10.2%, whereas δ_{AE} increases by 27.2%:

$$\gamma_{el} = \delta_{el} \cdot T. \tag{15}$$

As the exchange current density of the corresponding electrode is proportional to γ_{el} and therefore δ_{el}, it is increased by the same percentage. Thus, the cell performance is also directly impacted by the temperature dependency of δ_{el}. With the temperature dependency of δ_{el} being described by a linear function, this results in γ_{el} exhibiting a quadratic dependency on temperature.

The determined γ_{AE} exceeds γ_{FE} by 3 orders of magnitude, whereas [2] reported a difference of about 2 orders of magnitude. A comparison with the temperature-independent values of δ_{el} of [2] is done in two ways. First, the mean values of the three δ_{el} determined here yield a δ_{FE} smaller by a factor of 3 and a δ_{AE} larger by a factor of 17 compared to [2]. Second, the extrapolation of the found temperature dependencies to 800 °C as used in [2] shows a smaller difference for δ_{FE} with a factor of 5, whereas for δ_{AE}, the difference increases to a factor of 24.

These differences in γ_{AE} likely stem from the different materials, suggesting superior performance of the LSC electrode compared to the LSCF electrode of [2]. The small difference in γ_{FE}, despite identical fuel electrode composition, may result from microstructural and stoichiometric variations.

3.3.4. Charge transfer coefficient α

After discussing the parameters determined from the EIS measurements at the OCV, the apparent charge transfer coefficient is determined from the EIS measurements recorded under load as described in [2]. To this end, current density variations are conducted at constant gas composition and temperature in both fuel cell and electrolysis operation mode. Gas compositions are set to $H_2/H_2O = 50/50$ and $O_2/N_2 = 21/79$ for the respective electrodes, and the current densities are selected as shown in table 2.

For each current density of table 2, resistances attributed to the electrochemical processes of each electrode are determined via CNLS fits. The resulting data are fitted with polynomial functions, which are

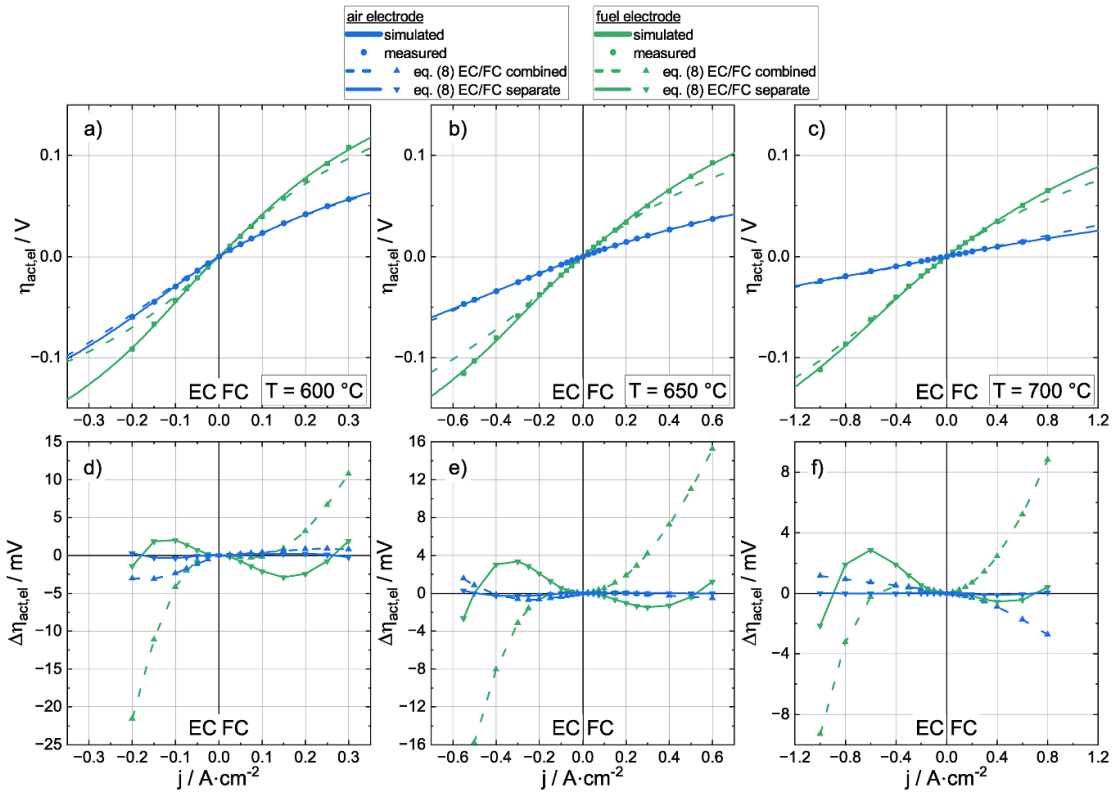

Figure 8. Comparison of experimentally determined activation overpotentials $\eta_{act,el}$ (symbols) with their simulated counterparts using two different Butler–Volmer-type approaches (lines) as a function of current density at (a) T = 600 °C, (b) 650 °C, and (c) 700 °C. The resulting difference of $\eta_{act,el}$ between experimental and simulated value $\Delta\eta_{act,el}$ is shown in (d) T = 600 °C, (e) 650 °C, and (f) 700 °C. Dashed lines represent the combined fit of fuel cell and electrolysis data utilizing one α, whereas solid lines represent the separate fit of each operation mode. Fuel electrode (green) and air electrode (blue) are distinguished by color.

then integrated to obtain expressions for the dependency of the activation overpotentials on current density. These, in turn, are evaluated at chosen current densities to provide overpotential data that can be fitted by equation (8) [2], using either the entire current density range at once or splitting it into positive and negative values. Exchange current densities $j_{0,el}$ are fixed via equation (9), leaving α_{el} as the sole fitting parameter, either as a single value for both EC and FC modes or as two separate values. The so-obtained activation overpotentials, as well as the corresponding fits, are presented in figure 8. The resulting values of α are presented in table 4 and appendix 2.

In general, figure 8 shows that the activation overpotential is less accurately predicted for the fuel electrode compared to the air electrode. Employing a single value for α_{FE} to describe $\eta_{act,FE}$ for both operation modes leads to higher errors at all three temperatures with errors increasing exponentially toward high absolute values of j. In contrast, while utilizing two separate values for α per electrode, the largest errors are found at medium current densities. Also, the maximum error is more than halved while allowing for the operation of mode-wise charge transfer coefficients.

For the activation overpotential of the air electrode $\eta_{act,AE}$, errors are found to be considerably smaller at all three temperatures. Benefits of assuming separate values of α_{AE} with respect to the operation mode can still be identified, particularly in the FC mode at 700 °C and in the EC mode at 600 °C.

The comparison provides evidence that for an accurate description of the experimentally determined activation losses, separate values for the charge transfer coefficients α are required that differentiate between the operation modes. At first, this may seem like a contradiction to the fact that, from a macroscopic perspective, EC and FC modes are merely two directions of the same reaction. However, it can be taken as an indication for a change in the microscopic conditions affecting the overall electrochemical reaction. For example, changes in the oxidation state of the electrode material [24, 38] or differences in potentials at the electrodes [39] may occur depending on the current direction and applied voltage and may affect the individual steps involved in the charge transfer reactions. Also, the influence of impurities can affect both operating modes in different manners [40, 41].

The results presented in figure 8 demonstrate that the use of the Butler–Volmer-type equation in this phenomenological manner yields a reasonably good accuracy with respect to the representation of the

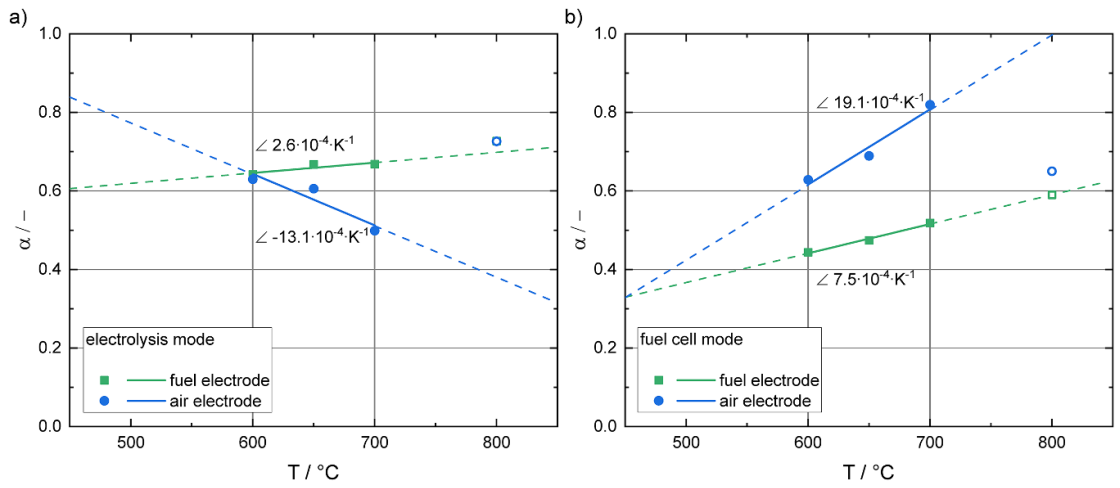

Figure 9. Determined values of α for both electrodes as a function of temperature in (a) electrolysis mode and (b) fuel cell mode. Values determined by suitable current density variation are shown as symbols at their respective temperature for the investigated cell (full) and the one investigated in [42] for electrolysis and in [2] in fuel cell mode (empty). Linear fits for the temperature dependency of the investigated cell are included as solid interpolation lines within the measured temperature range and as dashed extrapolation lines for temperatures outside the measured range.

activation losses despite the violation of critical assumptions underlying its derivation. Further variants of the equation, for example, with independent charge transfer coefficients for the forward and backward reactions, were also tested, but did not show any improvement over the chosen case. Moreover, obtaining meaningful fitting results proved challenging with such variants, especially for the air electrode at 700 °C. This is attributed to the form of the equation for j_0 changing for two independent charge transfer coefficients α_1 and α_2 (instead of α and $(1-\alpha)$ in equation (8)). While linearizing the general form of the Butler–Volmer equation, an additional factor of $1/(\alpha_1+\alpha_2)$ is introduced into equation (9). Therefore, j_0 cannot be determined independently of α as it is when the constraint $\alpha_1+\alpha_2=1$ is applied. As a result, j_0 is not solely a measure for the conditions at OCV, and the values for α also impact the current density for $\eta_{\mathrm{act}}=0$.

Including the additional α-dependent factor for the determination of j_0 does not change the number of fit parameters while determining α. Nonetheless, the shape of the Butler–Volmer-type equation, especially the slope at low activation overpotentials, is impacted by the values of α. Without strict boundaries for α_1, α_2, and j_0, this results in the values of these parameters being difficult to interpret.

Since the variant with operational mode-wise charge transfer coefficients yields the most accurate fits with experimental data, this variant is selected in this work to investigate the temperature dependency of the charge transfer coefficient. Temperature-dependent values for the respective α resulting from this approach are shown in figure 9 and further discussed in detail in the following.

Comparing the values of figures 9(a) and (b), one finds that the value of α_{FE} for the fuel electrode is generally larger in the EC mode than in the FC mode. For example, at 600 °C, respective values of the charge transfer coefficient are $\alpha_{\mathrm{FE,EC}}=0.642$ and $\alpha_{\mathrm{FE,FC}}=0.444$. With increasing temperature, the relative difference becomes slightly smaller from +30.8% at 600 °C down to +22.5% at 700 °C due to a stronger increase in fuel cell mode values with temperature.

The opposite trend is found for the air electrode, where $\alpha_{\mathrm{AE,EC}}$ is either smaller than (at 650 °C and 700 °C) or similar to $\alpha_{\mathrm{AE,FC}}$ (600 °C). Furthermore, the relative difference between $\alpha_{\mathrm{AE,EC}}$ and $\alpha_{\mathrm{AE,FC}}$ is increasing noticeably with temperature, from −19.9% at 650 °C to −64.5% at 700 °C.

Values of α that differ from 0.5 have opposing effects on the performance under fuel cell and electrolysis operation, as shown in figure 10.

In the fuel cell mode, the current density is defined positive; thus, a high value for the forward current density (the first term in the brackets of equation (8)) is desired. This is favored by large values of α, as in this case smaller values of the overpotential η_{act} are required to induce the same forward current density. The undesired backwards reaction (the second term in the brackets of equation (8)) also increases with α, but only to a minor extent, therefore resulting in an overall increase in the net current density. For the electrolysis mode, large magnitudes of the backward reaction are sought. Here, the same argument as above applies to the term $(1-\alpha)$ due to the negative value of the overpotential. Hence, to maximize the backward reaction, small values of α are beneficial. To conclude, $\alpha>0.5$ indicates better performance in the fuel cell mode, whereas $\alpha<0.5$ hints at enhanced performance for the electrolysis mode.

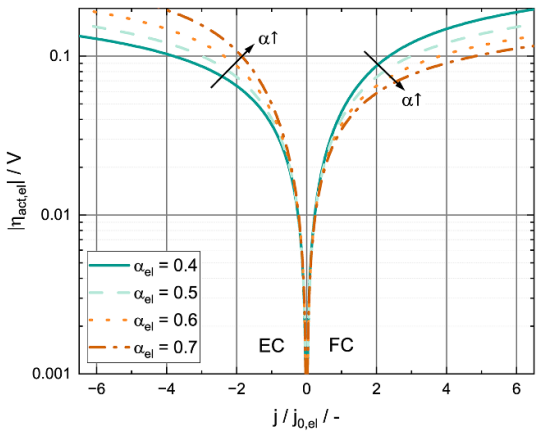

Figure 10. Exemplary depiction of the activation overpotential $\eta_{act,el}$ as a function of the ratio of current density j and exchange current density $j_{0,el}$ for different charge transfer coefficients α_{el}, calculated via equation (8) for a temperature of 700 °C.

Following this argumentation and considering the values of α_{AE} given in figure 9, it is found that, with one exception (700 °C) – fuel cell operation, that is the reduction of oxygen, is the favored reaction direction of the air electrode. At 700 °C, the values of $\alpha_{AE,EC}$ (0.498) and $\alpha_{AE,FC}$ (0.819) differ significantly. This disparity may be a consequence of a change in the local reaction conditions (electrical double layer, partial pressures, etc) and the different reduction states of LSC and thus ionic conductivity and surface exchange rate changes due to the applied loads. This difference is less pronounced for lower temperatures.

For the fuel electrode, $\alpha_{FE,FC}$ lies below 0.5 for 600 °C and 650 °C in the fuel cell mode, whereas in the electrolysis mode $\alpha_{FE,FC}$ is larger than 0.5. This means that in either mode, the desired reaction direction with respect to the operation is not the one favored by the electrode kinetics. The only exception is found for $\alpha_{FE,FC}$ at 700 °C (0.518), where the hydrogen oxidation seems at least slightly preferred over the steam reduction.

While the absolute levels of activation losses of the individual electrodes are primarily determined by the magnitude of the respective exchange current densities, the variations of their ratio with applied current density is affected by the values of the charge transfer coefficients. Considering the findings described above, one can therefore conclude that for the cells investigated in this work, the activation overpotential at the air electrode becomes smaller relative to that at the fuel electrode with increasing current density, both in EC and FC mode.

The temperature dependency of α over the investigated temperature range is described using a linear function, as shown in figure 9. In particular, for air electrodes, the linear trend does not match all data points perfectly. However, due to the low number of points needed to fit and lack of physically motivated reason to use higher order polynomials, we refrain from more complex fit functions.

In both the EC and FC modes, α_{AE} shows a stronger dependency on temperature than α_{FE}, as expressed by the absolute values of the respective slopes. In the electrolysis mode, the slope of the temperature dependency of $\alpha_{AE,EC}$ is $-13.1 \cdot 10^{-4}$ K^{-1} and therefore about five times larger than the one of $\alpha_{FE,EC}$ ($2.6 \cdot 10^{-4}$ K^{-1}). In the fuel cell mode, a factor of 2.5 between the slope of the temperature dependency of $\alpha_{AE,FC}$ ($19.1 \cdot 10^{-4}$ K^{-1}) compared to $\alpha_{FE,FC}$ ($7.5 \cdot 10^{-4}$ K^{-1}) is found. A similar slope for $\alpha_{FE,FC}$ of $8.0 \cdot 10^{-4}$ K^{-1} was determined by [43] for patterned Ni on YSZ electrodes in the temperature range of 700 °C–800 °C. In large stacks, where internal temperatures may differ locally by more than 100 °C [23, 44], such pronounced temperature dependencies can result in substantial inhomogeneities in the current and overpotential distribution at the air electrodes of individual cells in the stack, potentially accompanied by unevenly accelerated aging.

Comparison of the deduced charge transfer coefficients with the values in [2] is limited to fuel cell operation since electrolysis operation is not considered in their work. Also, in [2], coefficients are only determined at 800 °C. For this condition, their fuel electrode value ($\alpha_{FE} = 0.59$) is higher, whereas their air electrode value ($\alpha_{AE} = 0.65$) is lower except for $T = 600$ °C than the ones found in this work. For a direct comparison at a common temperature, the temperature trends found above are extrapolated to 800 °C. This leads to a value of $\alpha_{FE,FC} = 0.595$ for the investigated cell, which is almost identical to the one determined by [2]. For the air electrode, the proposed extrapolation would yield $\alpha_{AE,FC} = 0.997$ for 800 °C, which is roughly 35% higher than $\alpha_{AE,FC} = 0.65$ determined by [2]. This would mean that in fuel cell operation, the kinetics of the investigated cell are significantly better than for the cell investigated in [2].

Extrapolated values of the charge transfer coefficient α_{EC} in electrolysis mode at 800 °C are compared with those from [42], which examines the same type of cell used in [2]. Again, similar coefficients are observed for the fuel electrode, with a value for $\alpha_{FE,EC} = 0.694$ that is only 4.5% smaller value than $\alpha_{FE,EC} = 0.727$ in [42]. In contrast, the difference of 47.7% for the air electrode is quite significant, with the investigated cell showing a smaller value of $\alpha_{AE,EC} = 0.380$ compared to $\alpha_{AE,EC} = 0.726$ in [42]. As mentioned earlier, both the similarities and discrepancies can be explained by the choice of electrode materials of the two cells, which is similar on the fuel side, but differ on the air side.

In particular, at high absolute current densities, the impact of the charge transfer coefficients on activation losses is not to be underestimated (figure 10). Using equation (8) in the limit of large currents, that is, in a regime where the backward reaction becomes negligible and assuming two electrodes that differ only by their charge transfer coefficients α and α' and otherwise share the same parameters, it can be shown that the activation losses at the respective electrodes are related by $\eta'_{act}/\eta_{act} = \alpha/\alpha'$. In other words, if the exchange current density of two electrodes is identical, the ratio of the activation losses generated while applying the same large current density is given by the ratio of their charge transfer coefficients.

4. Validation

The derived parameters (cf table 3 and 4) are implemented in a 0D model, as presented in [2, 4], which allows the computation of the cell voltage at a given current density by first evaluating the OCV at a set of operating conditions (equation (16)) and then subtracting all relevant overpotentials (equation (17)). Ohmic, diffusion, and conversion overpotentials are hereby given by equations (18)–(22) and can be computed directly by the insertion of the desired current density. Activation overpotentials are calculated via equation (23), together with equations (24) and (25). Since equation (23) cannot be inverted analytically, either the interpolation of results from a set of overpotentials or numerical inversion is used to determine the overpotential at the desired current density. Temperatures are taken as predefined and enter the calculation via the temperature dependencies of the various coefficients in equations (23)–(25). The parameterization is validated by the comparison of calculated current–voltage curves to measured data:

$$U_{OCV} = \frac{-\Delta G_0}{2F} - \frac{RT}{2F}\ln\left(\frac{pH_2O}{pH_2 \cdot \sqrt{pO_2}}\right) \tag{16}$$

$$U_{cell} = U_{OCV} - (\eta_{ohm} + \eta_{act,FE} + \eta_{act,AE} + \eta_{diff,FE} + \eta_{diff,AE} + \eta_{conv,FE} + \eta_{conv,AE}) \tag{17}$$

$$\eta_{ohm} = j \cdot R_{ohm}(T) \tag{18}$$

$$\eta_{diff,FE} = \frac{RT}{2F} \cdot \ln\left(\frac{1 + \frac{RTL_{FE}}{2F\psi_{FE} D_{mol,H_2O} pH_2O} \cdot j}{1 - \frac{RTL_{FE}}{2F\psi_{FE} D_{mol,H_2} pH_2} \cdot j}\right) \tag{19}$$

$$\eta_{diff,AE} = \frac{RT}{4F} \cdot \ln\left(\frac{1}{1 - \frac{RTL_{AE}}{4F\psi_{AE} D_{mol,O_2} pO_2} \cdot j}\right) \tag{20}$$

$$\eta_{conv,FE} = \frac{RT}{8F^2 J_{FE}} \cdot \left(\frac{1}{x_{H2}} + \frac{1}{x_{H2O}}\right) \cdot j \tag{21}$$

$$\eta_{conv,AE} = \frac{RT}{4F^2 J_{AE}} \cdot \left(\frac{1}{x_{O2}} + \frac{1}{x_{N2}}\right) \cdot j \tag{22}$$

$$j = j_{0,el}\left(e^{\left(\alpha_{el}(T)\frac{n_e F \eta_{act,el}}{RT}\right)} - e^{\left(-(1-\alpha_{el}(T))\frac{n_e F \eta_{act,el}}{RT}\right)}\right) \tag{23}$$

$$j_{0,FE} = \delta_{FE}(T) \cdot T \cdot \left(\frac{pH_2}{p_{atm}}\right)^{a(T)} \left(\frac{pH_2O}{p_{atm}}\right)^{b(T)} \cdot e^{\left(-\frac{E_{act,FE}}{RT}\right)} \tag{24}$$

$$j_{0,AE} = \delta_{AE}(T) \cdot T \cdot \left(\frac{pO_2}{p_{atm}}\right)^{m(T)} \cdot e^{\left(-\frac{E_{act,AE}}{RT}\right)}. \tag{25}$$

Table 3. Temperature-independent parameters determined within the temperature range of 500°C–750 °C or at 700 °C (ψ_{el}).

Parameter	Value
B_{AE} ($S^{-1}\cdot m^2$)	$2.06 \cdot 10^{-14}$
$E_{act,AE}$ ($kJ\cdot mol^{-1}$)	152.8
B_{FE} ($S^{-1}\cdot m^2$)	$3.70 \cdot 10^{-11}$
$E_{act,FE}$ ($kJ\cdot mol^{-1}$)	101.4
B_{ohm} ($S\cdot K\cdot m^{-2}$)	$6.41 \cdot 10^{12}$
$E_{act,ohm}$ ($kJ\cdot mol^{-1}$)	92.6
ψ_{FE} (-)	0.037
ψ_{AE} (-)	0.028

Table 4. Kinetic parameters determined by variations of the operating conditions at 600 °C, 650 °C, and 700 °C.

T (°C)	600	650	700
a (-)	−0.08	−0.046	−0.011
b (-)	0.12	0.168	0.191
γ_{FE} ($A\cdot m^{-2}$)	$1.20 \cdot 10^6\cdot T\cdot K^{-1}$	$1.27 \cdot 10^6\cdot T\cdot K^{-1}$	$1.32 \cdot 10^6\cdot T\cdot K^{-1}$
$\alpha_{FE,EC}$ (-)	0.642	0.667	0.668
$\alpha_{FE,FC}$ (-)	0.444	0.474	0.518
m (-)	0.106	0.185	0.26
γ_{AE} ($A\cdot m^{-2}$)	$2.47 \cdot 10^9\cdot T\cdot K^{-1}$	$2.79 \cdot 10^9\cdot T\cdot K^{-1}$	$3.14 \cdot 10^9\cdot T\cdot K^{-1}$
$\alpha_{AE,EC}$ (-)	0.629	0.605	0.498
$\alpha_{AE,FC}$ (-)	0.628	0.689	0.819

4.1. Prediction of various operating conditions

The model's ability to accurately predict the cell performance for different fuel gas compositions is investigated for binary and ternary gas mixtures at the three temperatures used for parameterization (figure 11). For the binary case, H_2O, and accordingly H_2, is varied between 10% and 90%. In fuel cell operation, the maximum error is observed for the fuel gas mixture of $H_2/H_2O = 90/10$, amounting to −7.8% for both 600 °C and 700 °C and −9.6% for 650 °C. In electrolysis operation, the maximum error is smaller, lying between −4.6% ($H_2/H_2O = 90/10$) and 1.9% ($H_2/H_2O = 10/90$) for 700 °C. It is worth noting that in electrolysis operation with binary gas mixtures, with the exception of $H_2/H_2O = 10/90$, the cell voltage tends to be underestimated at higher electrolysis current densities or likewise performance slightly overestimated. In fuel cell operation at all temperatures, the cell voltage is underestimated. The only exception is a fuel gas mixture of $H_2/H_2O = 50/50$ at 700 °C, where the error is close to zero.

Ternary gas compositions including N_2 are selected to assess model accuracy in the case of fuel starvation. The according diffusion coefficients for the ternary gas mixture are evaluated for H_2, H_2O, and N_2 via equations (3)–(6). The model satisfactorily reproduces the cell performance, with errors below ±8.7% across all temperatures and ternary mixtures. The largest error values are observed at high current densities, whereas for moderate current densities, the errors are similar to those found for the binary case.

The increasing error between measurements and simulations with larger current densities may be attributed at least partially to the imprecise representation of microstructural effects and the simple gas diffusion resistance model employed (equations (19) and (20)). The microstructure is a decisive factor for diffusion overpotentials, which dominate at high current density. Hence, a precise description determines how accurate the limiting current can be represented. In this model, the microstructure of each electrode is represented by the parameters ψ_{AE} and ψ_{FE}. To deduce these parameters, the values for the mean pore radius of each electrode had to be adopted from the literature [23]. Thus, deviations between the determined and actual values of ψ_{el} are not unexpected. Moreover, according to the literature, a precise depiction of the gas diffusion losses in porous SOC electrodes requires at least a spatial resolution in two dimensions [45, 46] and a more complex gas diffusion model such as the Dusty–Gas model [45, 47], compared to the Ficks model including the Bosanquet approach applied here.

Furthermore, the endothermic electrolysis and exothermic fuel cell operations cool and heat up the cell under load, respectively. Since the model is isothermal and is not corrected for temperature changes under load, this introduces an additional source of error [4]. The resulting overestimation of the local temperature should lead to a better performance in the electrolysis mode predicted by the model, at least up to the thermoneutral voltage of 1.29 V. In the fuel cell mode, the model is expected to underestimate performance

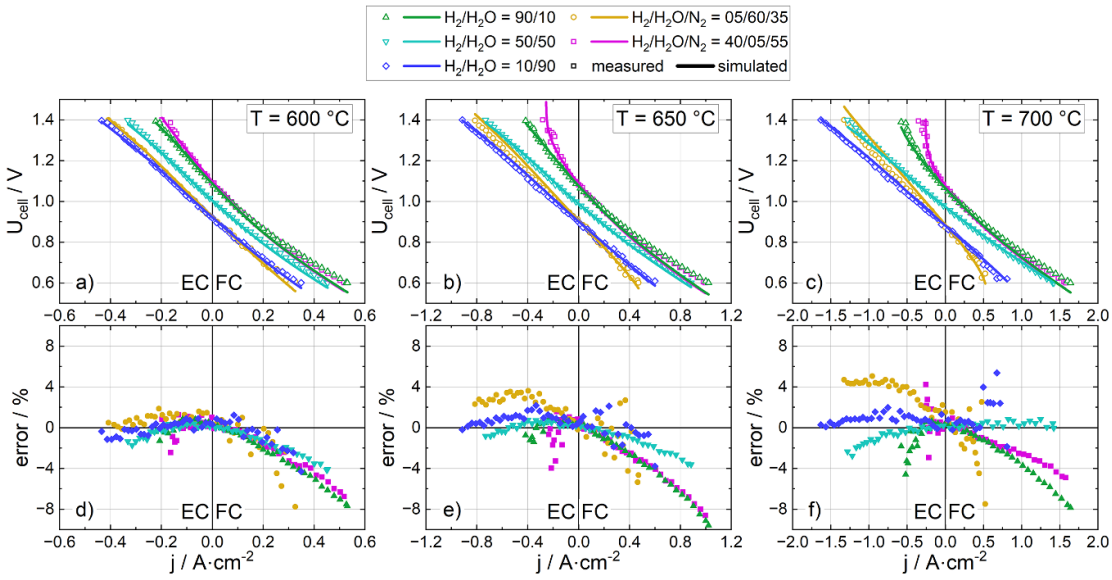

Figure 11. Current–voltage (*CV*) curves at (a) $T = 600$ °C, (b) 650 °C, and (c) 700 °C for three binary and two ternary fuel gas mixtures with a total fuel gas flow rate $\dot{V}_{\text{fuel}} = 0.605$ nlm and total air flow rate $\dot{V}_{\text{oxidant}} = 1.283$ nlm at $p_{\text{atm}} = 1$ atm and $A_{\text{active}} = 1.03$ cm^2. Corresponding values of the errors between simulation and measurement are given in (d) $T = 600$ °C, (e) 650 °C, and (f) 700 °C.

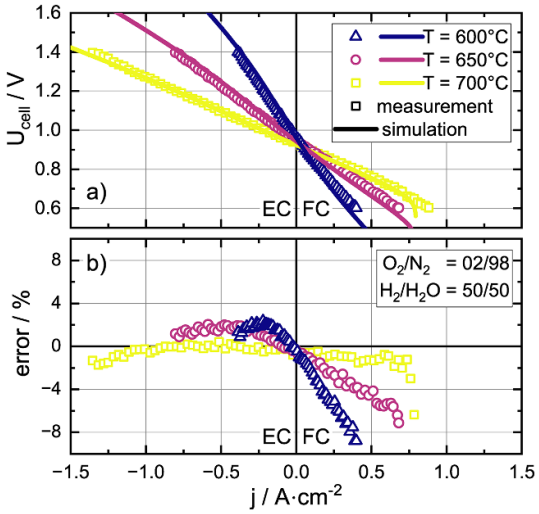

Figure 12. (a) Current–voltage (*CV*) curves and (b) error between simulated and measured *CV* curves for a gas mixture of $O_2/N_2 = 02/98$ and $H_2/H_2O = 50/50$ at $T = 600$ °C, 650 °C, and 700 °C with a total fuel gas flow rate $\dot{V}_{\text{fuel}} = 0.605$ nlm and total air flow rate $\dot{V}_{\text{oxidant}} = 1.283$ nlm at $p_{\text{atm}} = 1$ atm and $A_{\text{active}} = 1.03$ cm^2.

since the actual temperature of the cell is increased by both joule heating and exothermic hydrogen oxidation reaction. This presumption is confirmed in almost all the investigated cases.

The model's accuracy under the conditions of oxygen starvation is tested using an O_2/N_2 ratio of 2/98 (figure 12). The analysis commences with electrolysis operation since, in this case, oxygen is a product of electrochemical reactions and low O_2 concentrations should therefore be less critical. Almost linear current voltage curves with low errors of $<2.5\%$ for 600 °C and 650 °C and -2% for 700 °C between model and measurements are observed. Both errors for lower and higher temperatures must be put into contrast with those obtained at conditions without the undersupply of oxygen, that is the case of $O_2/N_2 = 21/79$ and $H_2/H_2O = 50/50$ shown in the cyan graphs of figure 11. First, the slightly positive error for $O_2/N_2 = 2/98$ at 600 °C and 650 °C seems to overcompensate with the negative error found for $O_2/N_2 = 21/79$, indicating that the losses at the air electrode at small oxygen levels are rather overestimated. Second, an increase in the error for larger current densities at 700 °C is found at both ordinary and low oxygen concentrations. Hence, it is likely a result of high gas conversion at the fuel electrode and is independent of the set O_2 concentration.

Table 5. Temperature dependencies of kinetic parameters determined for the temperature range of 600 °C–700 °C.

Parameter	Expression
$a(T)$	$-0.080\,17 + 6.9 \cdot 10^{-4}\cdot\mathrm{K}^{-1}\cdot(T - 873.15\ \mathrm{K})$
$b(T)$	$0.124\,17 + 7.1 \cdot 10^{-4}\cdot\mathrm{K}^{-1}\cdot(T - 873.15\ \mathrm{K})$
$m(T)$	$0.105\,67 + 15.4 \cdot 10^{-4}\cdot\mathrm{K}^{-1}\cdot(T - 873.15\ \mathrm{K})$
$\gamma_{\mathrm{FE}}(T) = \delta_{\mathrm{FE}}(T)\cdot T$	$(1.201\,142 \cdot 10^{6} + 1.221 \cdot 10^{3}\cdot\mathrm{K}^{-1}\cdot(T - 873.15\ \mathrm{K}))\cdot T\cdot\mathrm{A}\cdot\mathrm{m}^{-2}\cdot\mathrm{K}^{-1}$
$\gamma_{\mathrm{AE}}(T) = \delta_{\mathrm{AE}}(T)\cdot T$	$(2.4601 \cdot 10^{9} + 6.70 \cdot 10^{6}\cdot\mathrm{K}^{-1}\cdot(T - 873.15\ \mathrm{K}))\cdot T\cdot\mathrm{A}\cdot\mathrm{m}^{-2}\cdot\mathrm{K}^{-1}$
$\alpha_{\mathrm{FE,EC}}(T)$	$0.642\,44 + 2.6 \cdot 10^{-4}\cdot\mathrm{K}^{-1}\cdot(T - 873.15\ \mathrm{K})$
$\alpha_{\mathrm{AE,EC}}(T)$	$0.642\,03 – 13.1 \cdot 10^{-4}\cdot\mathrm{K}^{-1}\cdot(T - 873.15\ \mathrm{K})$
$\alpha_{\mathrm{FE,FC}}(T)$	$0.445\,33 + 7.5 \cdot 10^{-4}\cdot\mathrm{K}^{-1}\cdot(T - 873.15\ \mathrm{K})$
$\alpha_{\mathrm{AE,FC}}(T)$	$0.615\,14 + 19.1 \cdot 10^{-4}\cdot\mathrm{K}^{-1}\cdot(T - 873.15\ \mathrm{K})$

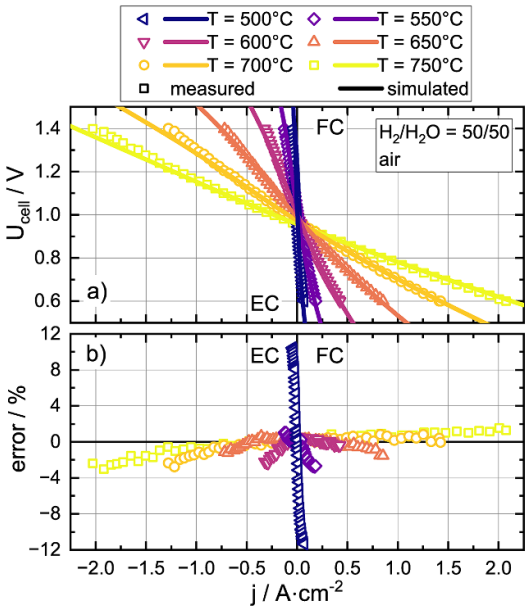

Figure 13. (a) Current–voltage (*CV*) curves and (b) error between simulated and measured *CV* curves using extrapolated values for temperature-dependent parameters (table 5) for a variation of temperature between 500°C and 750°C and a gas mixture of $H_2/H_2O = 50/50$ and $O_2/N_2 = 21/79$ (air) with a total fuel gas flow rate $\dot{V}_{\mathrm{fuel}} = 0.605$ nlm and total air flow rate $\dot{V}_{\mathrm{oxidant}} = 1.283$ nlm at $p_{\mathrm{atm}} = 1$ atm and $A_{\mathrm{active}} = 1.03\ \mathrm{cm}^2$.

During fuel cell operation, the impact of O_2 starvation becomes visible at lower current densities reached at the same cell voltage. For example, at for $U_{\mathrm{cell}} = 0.6$ V and $T = 600$ °C, the obtained current density is 0.4 A·cm^{-2} at $O_2/N_2 = 2/98$, whereas it is 0.45 A·cm^{-2} at $O_2/N_2 = 21/79$. Absolute errors between the model and the measurement reach maximum values of 8.7%, with the measured cell voltage being underestimated by the model. The limiting current, at which the cell performance descends rather abruptly, is underestimated for the temperatures investigated. Similar to what is discussed for the fuel electrode, this may be explained by the imprecise values of the microstructural factor ψ_{AE} and mean pore radius $r_{\mathrm{pore,AE}}$ as well as by a simple diffusion model applied. Inaccuracies while determining the air electrode thickness are also possible explanations for errors in the limiting current. As an example, a tolerance of only 2–3 μm corresponds to 10% of the total electrode thickness for the investigated cell and is due to the direct proportionality (equation (2)) thus also to an error of 10% in the diffusion resistance.

4.2. Extrapolation of kinetic parameters

The capability of the model to predict the cell performance at temperatures outside the parameterization range using extrapolated parameter values (table 5) is illustrated in figure 13. To achieve this, 500°C, 550°C, and 750°C were selected for temperatures below and above those used for the parameterization. A reasonably good agreement between the measurements and simulations is found for both 550°C and 750°C. For 750°C and at absolute current densities above 2 A·cm^{-2}, a maximum error of −3% in electrolysis and 1.5% in fuel cell mode is observed. The cell performance is thus slightly overestimated in both modes. For 550°C, a maximum error of 1.1% in electrolysis and −2.9% in the fuel cell mode is found, indicating a slight underestimation of cell performance. For 500°C, the measured current density range is limited to the range

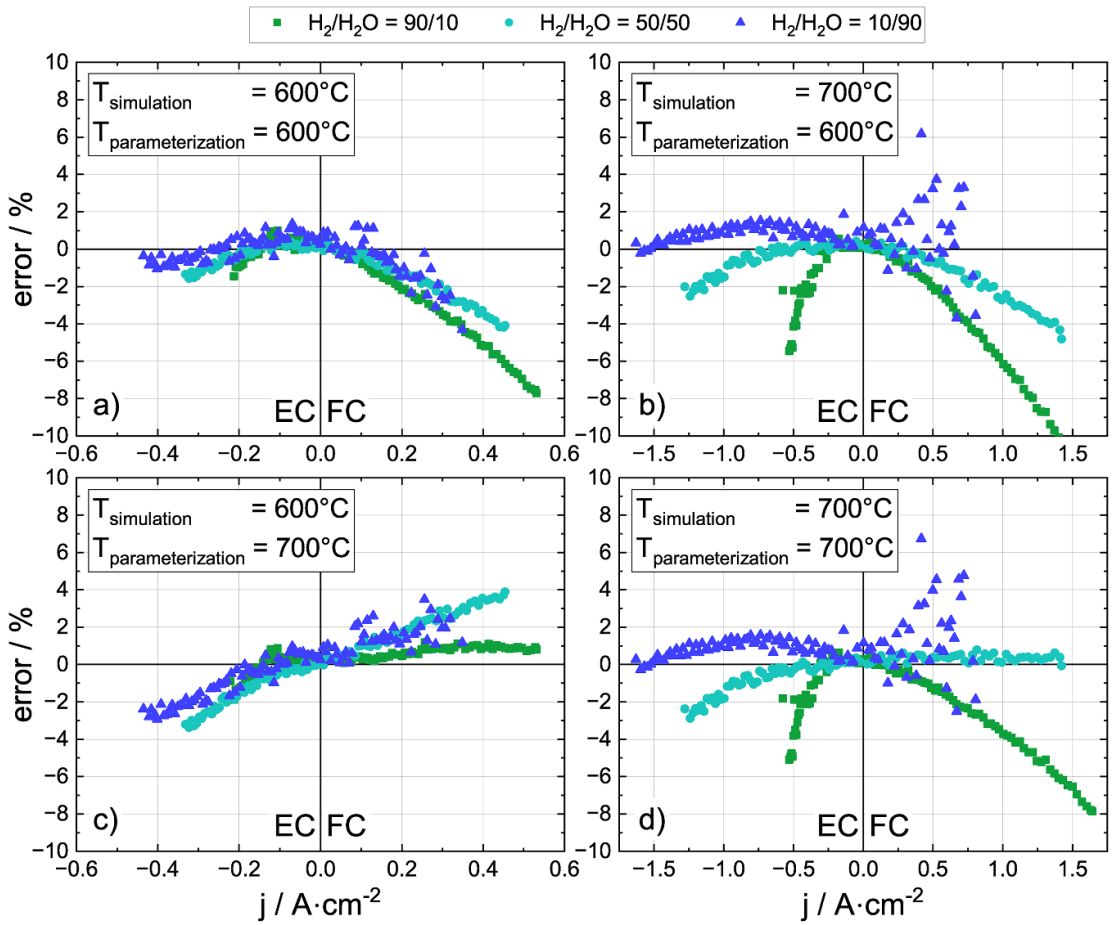

Figure 14. Errors between simulated and measured *CV* curves for (a) + (c) $T = 600$ °C and (b) + (d) $T = 700$ °C and parameter sets determined at (a) + (b) $T = 600$ °C and (c) + (d) $T = 700$ °C for a three binary fuel gas mixtures and $O_2/N_2 = 21/79$ (air) with a total fuel gas flow rate $\dot{V}_{\text{fuel}} = 0.605$ nlm and total air flow rate $\dot{V}_{\text{oxidant}} = 1.283$ nlm at $p_{\text{atm}} = 1$ atm and $A_{\text{active}} = 1.03$ cm^2.

between -0.045 A·cm^{-2} and 0.07 A·cm^{-2} due to the increased cell resistance. The maximum error is found to be quite large, with values of 10.5% in the electrolysis mode and -11.4% in the fuel cell mode. This corresponds to a significant underestimation of cell performance and sets limits on the temperature range where extrapolation of the extracted parameters is still valid.

4.3. Comparison of parameter sets

The benefit of the model accuracy while using temperature-dependent kinetic parameters is demonstrated in figure 14. Here, the agreement between simulation and measurement is compared for cases, where measurement and parameterization temperatures coincides, and cases, for which they differ. Three binary fuel gas mixtures are considered at each operation temperature.

For electrolysis operation at 600 °C, using parameters determined at 600 °C (figure 14(a)) leads to approximately half the error for both $H_2/H_2O = 50/50$ and 10/90 and a similar error for $H_2/H_2O = 90/10$ compared to the simulations with parameters determined at 700 °C (figure 14(c)). For fuel cell operation at 600 °C, the absolute value of the error for both $H_2/H_2O = 50/50$ and 10/90 is similar for both parameter sets. Surprisingly, the absolute value of the error for $H_2/H_2O = 90/10$ is significantly larger for the parameter set determined at 600 °C. In addition to the difference in absolute values, the derived errors differ with respect to their sign. The parameter set determined at 600 °C underestimates the cell voltage and thus performance, whereas the 700 °C parameter set overestimates both. An underestimation of the cell voltage in the fuel cell mode is expected, as described earlier, due to the cell generating heat during operation [4]. Corrections to this effect in a planned future nonisothermal model are expected to shift the predicted voltages to higher values. An overestimation of the cell voltage, as is the case for the 700 °C parameters, would then be even more magnified.

At an operation temperature of 700 °C, the two parameter sets yield similar results for electrolysis operation (figures 14(b) and (d)). In contrast, in fuel cell operation, noticeable differences between both parameter sets for $H_2/H_2O = 90/10$ and 50/50 are observed, with the parameter set determined at 700 °C,

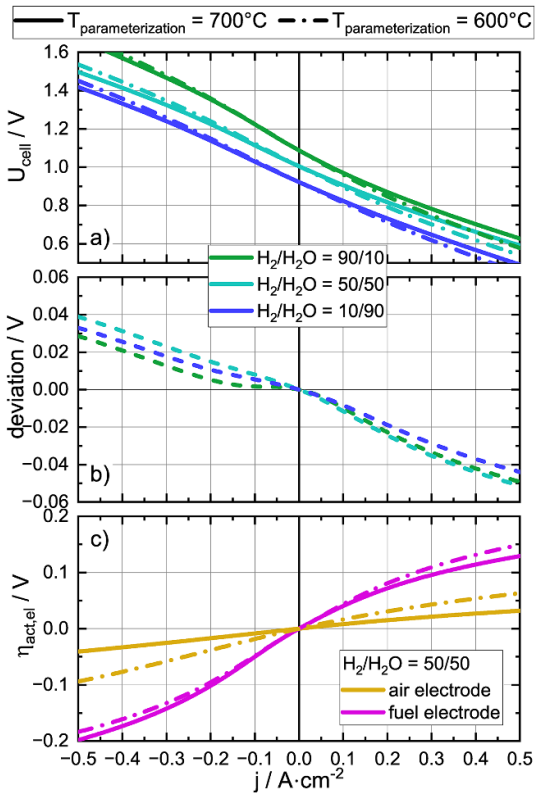

Figure 15. Comparison of simulations for a temperature of 600 °C conducted with parameter sets determined at 600 °C and 700 °C. (a) *CV* curves and (b) deviations between *CV* curves for the two parameter sets for three binary fuel gas mixtures and $O_2/N_2 = 21/79$ (air). (c) Comparison of activation overpotentials for the two parameter sets for a fuel gas mixture of $H_2/H_2O = 50/50$. The total fuel gas flow rate is set to $\dot{V}_{fuel} = 0.605$ nlm and total air flow rate $\dot{V}_{oxidant} = 1.283$ nlm, $p_{atm} = 1$ atm and $A_{active} = 1.03$ cm².

yielding smaller errors. The unequal impact of the parameter sets on the operating mode is attributed to the charge transfer coefficient α, as it is the only parameter specific to the operating mode. In the electrolysis mode, the temperature dependencies of α for both electrodes follow opposing trends, as shown in figure 9(a), with $\alpha_{FE,EC}$ increasing and $\alpha_{AE,EC}$ decreasing with temperature. For the parameter set determined at 700 °C, this leads to lower activation overpotentials at the air electrode and higher activation overpotentials at the fuel electrode compared to the 600 °C parameter set. Both effects thus compensate each other while considering the resulting overall cell voltage.

For fuel cell operation, both $\alpha_{AE,FC}$ and $\alpha_{FE,FC}$ increase with temperature (figure 9(b)), leading to lower activation overpotentials at both electrodes for parameters determined at 700 °C compared to the ones determined at 600 °C. In this case, the changes in overpotentials do not cancel out. Consequently, larger differences in the error (figure 14) can be observed.

While the sum of activation overpotentials may be comparable for both parameter sets, especially during electrolysis, the individual contribution of each electrode differs due to the temperature dependence of α. An accurate attribution of activation overpotentials to individual electrodes requires the consideration of this temperature dependence, particularly while incorporating overpotential-dependent aging mechanisms into the model.

The relatively small difference in errors between the two parameter sets for a gas composition of $H_2/H_2O = 10/90$ in the fuel cell mode can be attributed to the larger impact of the gas diffusion overpotential at the fuel electrode under these conditions. Undersupply of educts for electrochemical reactions already arises at low current densities, resulting in a larger contribution to the total overpotential that is attributed to gas diffusion. The microstructural parameters governing the diffusion overpotential, that is ψ_{el} and $r_{pore,el}$, are temperature-independent, and the calculated gas diffusion overpotentials also change little with temperature. In summary, this leads to a small difference between the results obtained with the two parameter sets. It should also be noted that the correct computation of diffusion losses is a general challenge for lower dimensional models. As an example, in [45, 46], it is discussed that at least two spatial dimensions are necessary to represent diffusion with reasonable accuracy. Thus, the model deficits with respect to a precise description of diffusion limitations remain, even if accurate microstructural parameters are available.

A further in-depth study of the two parameter sets, comparing the respective model predictions directly with each other, is presented in figure 15 for a temperature of 600 °C. The deviation between the calculated cell voltages for both parameter sets increases with current density for both operation modes. A difference in the cell voltage of up to 39 mV in electrolysis at -0.5 A·cm^{-2} and -51 mV in fuel cell operation at 0.5 A·cm^{-2} is apparent. Deviations between the predictions increase with current density when departing from OCV conditions but remain approximately constant for absolute current densities larger than ca. 0.2 A·cm^{-2} (figure 15(b)). This characteristic trend is likely to be caused by differences in the activation overpotentials, which is also supported by the fact that the parameters governing ohmic ($E_{\mathrm{act,ohm}}$ and B_{ohm}) and diffusion overpotentials (ψ_{el} and $r_{\mathrm{pore,el}}$) are the same for both parameter sets.

Figure 15(c) underlines this finding by a direct comparison of the activation overpotentials of both electrodes at a fuel gas composition of $H_2/H_2O = 50/50$. The usage of the parameters determined at 700 °C yields more than 50% lower air electrode activation overpotentials $\eta_{\mathrm{act,AE}}$ compared to the 600 °C parameter set at all current densities. For example, the activation overpotential at $j = -0.5$ A·cm^{-2} (0.5 A·cm^{-2}) amounts to only $\eta_{\mathrm{act,AE}} = -0.041$ V (0.032 V) at 700 °C, whereas it already becomes $\eta_{\mathrm{act,AE}} = -0.094$ V (0.063 V) at 600 °C.

For the fuel electrode activation overpotential $\eta_{\mathrm{act,FE,}}$ the relative deviation between both computations is smaller, with the 700 °C parameter set yielding a 7.8% higher overpotential in electrolysis and a 13.5% lower overpotential in the fuel cell mode.

This investigation establishes that using kinetic parameters at temperatures different from those at which they were determined can lead to deviations in the predicted overpotential contributions. As a result, neglecting the temperature dependency of these parameters may not only impact the predicted cell voltage but can also impair the accuracy of degradation models [48, 49] that built upon the results of the cell model and heavily rely on trustworthy calculations of the individual overpotentials. By measuring the actual cell temperature under load locally [4] and moving away from the isothermal assumption, an even greater accuracy in the prediction of cell voltage can be achieved.

5. Conclusion

Parametrization of a 0D cell model describing the electrochemical loss processes in an SOC was performed for a commercially available fuel electrode supported cell via EIS measurements using the approach presented in [2]. In contrast to previous work with temperature-independent kinetic parameters, the respective measurement series were conducted at three different temperatures ($T = 600$ °C, 650 °C, and 700 °C). It is found that the influence of temperature on cell performance is not limited to the designated temperature-comprising terms, for example, the Arrhenius exponents for the ohmic and electrode activation resistances and the proportionality factor γ of the exchange current density. Parameters are assumed to be temperature-independent in the state-of-the-art literature, for example, partial pressure dependency exponents *a, b, and m* of the exchange current densities, and the temperature prefactor δ_{el} as part of the proportionality factor γ_{el} of the exchange current densities, and charge transfer coefficients α in both electrolysis and fuel cell modes, were found to exhibit quantifiable temperature dependencies. In most cases, the temperature dependencies can be described by simple linear relations. By comparing both electrodes of the investigated cell, parameters describing the activation overpotential at the air electrode were found to exhibit a stronger dependency on temperature than parameters of the fuel electrode.

The benefits of employing accurately determined temperature dependencies for the kinetic parameters are examined by comparing a scenario where the parameterization temperature deviates by 100 K from the temperature in question with the case where both temperatures coincide.

In terms of the total cell voltage, slightly lower maximum errors (-5.1% vs. -5.4%) were found for the matching case. In fuel cell operation, the impact of accounting for the temperature dependency of the kinetic parameters is more complex, as the influence varies depending on the investigated temperature and fuel gas composition.

An accurate estimation of activation overpotentials is essential for the prediction of cell degradation and consequently for targeted improvements of cell and stack design with respect to performance and durability. Significant deviations while neglecting the temperature dependency of the kinetic parameters were found for the predicted activation overpotentials, with deviations of more than 50% for the air electrode and 13% for the fuel electrode.

The derived dependencies improve the agreement between simulation and measurement. It is expected that these improvements will become even more significant in the presence of substantial temperature differences. In particular, for systems of larger spatial extent, for example, large area cells or stacks with considerable temperature gradients of up to and beyond 100 K, either between the inlet and outlet of cells or

between the bottom, middle, and top cells in a stack, can be observed and may thus demand accurately modeled temperature dependencies.

Data availability statement

The data that support the findings of this study are available upon reasonable request from the authors.

Acknowledgment

We acknowledge Elcogen AS for supplying us with the commercially available cells and the Elcogen R&D team for the insightful discussions on cell properties.

Appendix 1.

The signs of the partial pressure exponents *a, b*, and *m* given in equations (10) and (11) determine whether $R_{\mathrm{act,el}}$ increases or decreases with changes in the respective partial pressure. This correlation is independent of the magnitude of the partial pressure. However, the question whether a certain shift in partial pressures induces smaller or larger changes in $R_{\mathrm{act,el}}$ depending on the corresponding exponent is more intricate as it is influenced by the absolute levels of the respective partial pressure (figure A1(a)). For better comparability, we thus consider only the relative slope (i.e., the slope of the variable divided by the value of the variable) of the exchange current density $j_{0,\mathrm{el}}$ or, likewise, the activation resistance $R_{\mathrm{act,el}}$ with respect to the partial pressure of a component. This, then, provides measure for the impact of the partial pressure exponent on the sensitivity of the activation resistance with respect to the corresponding partial pressure. The relation between this relative slope, the partial pressure p_i and the corresponding exponent x_i is deduced by the following steps:

$$\frac{1}{R_{\mathrm{act,el}}} \sim j_{0,\mathrm{el}} \sim {p_i}^{x_i}$$

$$\frac{\partial j_{0,\mathrm{el}}}{\partial p_i} \sim x \cdot {p_i}^{x-1}$$

$$\frac{\frac{\partial j_{0,\mathrm{el}}}{\partial p_i}}{j_{0,\mathrm{el}}} = \frac{x}{p_i}.$$

Hence, a larger absolute value of *a, b*, or *m* leads to a higher sensitivity of the exchange current density j_0 with respect to the partial pressure p_i of that the corresponding component *i* (figure A1(b)).

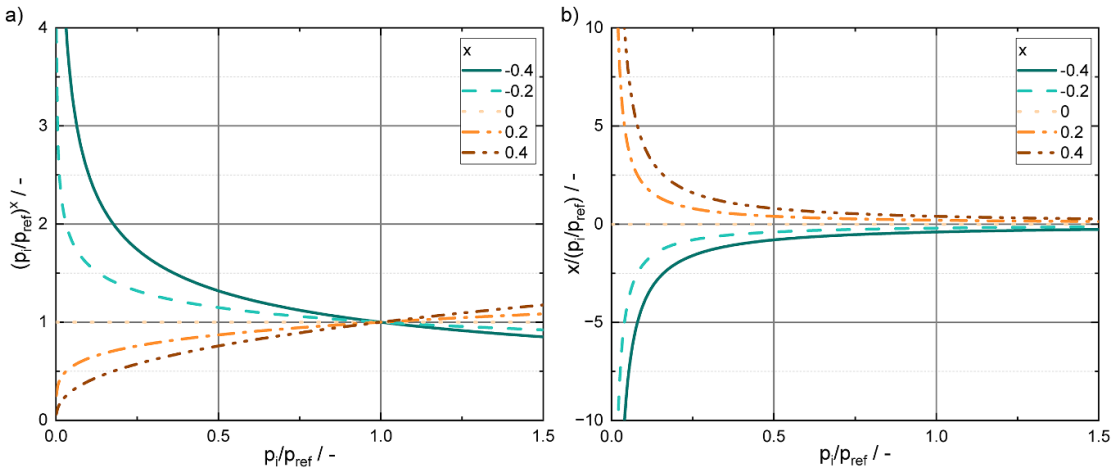

Figure A1. (a) Partial pressure dependent factor of the exchange current density and (b) the relative slope of the exchange current density as functions of the relative partial pressure for different partial pressure exponents x.

Appendix 2.

Table A1. Determined charge transfer coefficients by fitting equation (8) to experimentally determined activation overpotentials for the three investigated temperatures. α_{el} (left part of the table) are obtained by fitting both electrolysis and fuel cell mode simultaneously, whereas $\alpha_{el,EC}$ and $\alpha_{el,FC}$ (right part of the table) are obtained by fitting both modes independent of each other.

EC/FC mode simultaneously fitted			EC/FC mode separately fitted				
T (°C)	α_{AE}	α_{FE}	T (°C)	$\alpha_{AE,FC}$	$\alpha_{AE,EC}$	$\alpha_{FE,FC}$	$\alpha_{FE,EC}$
600	0.645	0.491	600	0.628	0.629	0.444	0.642
650	0.671	0.583	650	0.689	0.605	0.474	0.667
700	0.484	0.641	700	0.819	0.498	0.518	0.668

References

[1] Mueller M, Klinsmann M, Sauter U, Njodzefon J-C and Weber A 2024 High temperature solid oxide electrolysis—technology and modeling *Chem. Ing. Tech.* **96** 143–66
[2] Leonide A, Apel Y and Ivers-Tiffee E 2009 SOFC modeling and parameter identification by means of impedance spectroscopy *ECS Trans.* **19** 81–109
[3] Grosselindemann C, Kullmann F, Lehnert T, Fritz O, Fuchs F and Weber A 2023 Comparison of a solid oxide cell with nickel/gadolinium-doped ceria fuel electrode during operation with hydrogen/steam and carbon monoxide/carbon dioxide *Fuel Cells* **23** 442–53
[4] Njodzefon J-C, Klotz D, Kromp A, Weber A and Ivers-Tiffée E 2013 Electrochemical modeling of the current-voltage characteristics of an SOFC in fuel cell and electrolyzer operation modes *J. Electrochem. Soc.* **160** F313
[5] Grosselindemann C, Russner N, Dierickx S, Wankmüller F and Weber A 2021 Deconvolution of gas diffusion polarization in Ni/gadolinium-doped ceria fuel electrodes *J. Electrochem. Soc.* **168** 124506
[6] Njodzefon J-C, Graves C R, Mogensen M B, Weber A and Hjelm J 2016 Kinetic studies on state of the art solid oxide cells: a comparison between hydrogen/steam and reformate fuels *J. Electrochem. Soc.* **163** F1451–62
[7] elcogen 2024 Product sheet elcoCell®
[8] Boukamp B and Rossmacdonald J 1994 Alternatives to Kronig-Kramers transformation and testing, and estimation of distributions *Solid State Ion.* **74** 85–101
[9] Boukamp B A 1995 A linear Kronig-Kramers transform test for immittance data validation *J. Electrochem. Soc.* **142** 1885–94
[10] Adler S B 1998 Mechanism and kinetics of oxygen reduction on porous $La_{1-x}Sr_xCoO_{3-\delta}$ electrodes *Solid State Ion.* **111** 125–34
[11] Leonide A 2010 *SOFC Modelling and Parameter Identification by Means of Impedance Spectroscopy* (KIT Scientific Publishing)
[12] Paasch G, Micka K and Gersdorf P 1993 Theory of the electrochemical impedance of macrohomogeneous porous electrodes *Electrochim. Acta* **38** 2653–62
[13] Dierickx S, Mundloch T, Weber A and Ivers-Tiffée E 2019 Advanced impedance model for double-layered solid oxide fuel cell cermet anodes *J. Power Sources* **415** 69–82
[14] Zhu H, Kee R J, Janardhanan V M, Deutschmann O and Goodwin D G 2005 Modeling elementary heterogeneous chemistry and electrochemistry in solid-oxide fuel cells *J. Electrochem. Soc.* **152** A2427
[15] Yrjänä V 2022 DearEIS—a GUI program for analyzing impedance spectra *JOSS* **7** 4808
[16] Kim J, Virkar A V, Fung K-Z, Mehta K and Singhal S C 1999 Polarization effects in intermediate temperature, anode-supported solid oxide fuel cells *J. Electrochem. Soc.* **146** 69–78
[17] Leonide A, Sonn V, Weber A and Ivers-Tiffée E 2008 Evaluation and modeling of the cell resistance in anode-supported solid oxide fuel cells *J. Electrochem. Soc.* **155** B36
[18] Froment G F, De Wilde J and Bischoff K B 2011 *Chemical Reactor Analysis and Design* (Wiley)
[19] Cussler E L 1997 *Diffusion: Mass Transfer in Fluid Systems* (Cambridge University Press)
[20] Fairbanks D F and Wilke C R 1950 Diffusion coefficients in multicomponent gas mixtures *Ind. Eng. Chem.* **42** 471–5
[21] Bird R B, Stewart W E and Lightfoot E N 2002 *Transport Phenomena* (Wiley)
[22] Hirschfelder J O, Curtiss C F and Bird R B 1963 *Molecular Theory of Gases and Liquids* (Wiley)
[23] Russner N, Dierickx S, Weber A, Reimert R and Ivers-Tiffée E 2020 Multiphysical modelling of planar solid oxide fuel cell stack layers *J. Power Sources* **451** 227552
[24] Joos J 2017 *Microstructural Characterisation, Modelling and Simulation of Solid Oxide Fuel Cell Cathodes* (KIT Scientific Publishing)
[25] Wehrle L, Schmider D, Dailly J, Banerjee A and Deutschmann O 2022 Benchmarking solid oxide electrolysis cell-stacks for industrial power-to-methane systems via hierarchical multi-scale modelling *Appl. Energy* **317** 119143
[26] Kullmann F, Mueller M, Lindner A, Dierickx S, Mueller E and Weber A 2023 DRT analysis and transmission line modeling of ceria based electrodes for solid oxide cells *J. Power Sources* **587** 233706
[27] Sogaard M, Hendriksen P, Mogensen M, Poulsen F and Skou E 2006 Oxygen nonstoichiometry and transport properties of strontium substituted lanthanum cobaltite *Solid State Ion.* **177** 3285–96
[28] Tsoga A, Naoumidis A, Jungen W and Stöver D 1999 Processing and characterisation of fine crystalline ceria gadolinia–yttria stabilized zirconia powders *J. Eur. Ceram Soc.* **19** 907–12
[29] Szász J, Wankmüller F, Wilde V, Störmer H, Gerthsen D, Menzler N H and Ivers-Tiffée E 2018 Nature and functionality of $La_{0.58}Sr_{0.4}Co_{0.2}Fe_{0.8}O_{3-\delta}/Gd_{0.2}Ce_{0.8}O_{2-\delta}/Y_{0.16}Zr_{0.84}O_{2-\delta}$ interfaces in SOFCs *J. Electrochem. Soc.* **165** F898–906
[30] Mogensen M, Frandsen H, Nielsen J, Li W, Jacobsen T and Graves C 2013 Current density—overvoltage relations for solid oxide electrodes *Proc. of the Smart Energy Conversion and Storage Conf.: IV Polish Forum (Krynica, Poland)* pp 1–4
[31] Bockris J O and Nagy Z 1973 Symmetry factor and transfer coefficient. A source of confusion in electrode kinetics *J. Chem. Educ.* **50** 839
[32] Lee W Y, Wee D and Ghoniem A F 2009 An improved one-dimensional membrane-electrode assembly model to predict the performance of solid oxide fuel cell including the limiting current density *J. Power Sources* **186** 417–27
[33] Bessler W G, Vogler M, Störmer H, Gerthsen D, Utz A, Weber A and Ivers-Tiffée E 2010 Model anodes and anode models for understanding the mechanism of hydrogen oxidation in solid oxide fuel cells *Phys. Chem. Chem. Phys.* **12** 13888

[34] Noren D A and Hoffman M A 2005 Clarifying the Butler–Volmer equation and related approximations for calculating activation losses in solid oxide fuel cell models *J. Power Sources* **152** 175–81
[35] Bessler W G, Gewies S and Vogler M 2007 A new framework for physically based modeling of solid oxide fuel cells *Electrochim. Acta* **53** 1782–800
[36] Momma A, Takano K, Tanaka Y, Kato T and Yamamoto A 2013 Experimental investigation of the effect of operating pressure on the performance of SOFC and SOEC *ECS Trans.* **57** 699–708
[37] Grosselindemann C, Dorn M, Bauer F M, Seim M, Ewald D, Esau D, Geörg M, Rössler R, Pundt A and Weber A 2024 Pressurized single cell testing of solid oxide cells *J. Power Sources* **614** 234963
[38] Atkinson A, Baron S A and Brandon N P 2004 AC impedance spectra arising from mixed ionic electronic solid electrolytes *J. Electrochem. Soc.* **151** E186
[39] Bessler W, Warnatz J and Goodwin D 2007 The influence of equilibrium potential on the hydrogen oxidation kinetics of SOFC anodes *Solid State Ion* **177** 3371–83
[40] Mogensen M B *et al* 2019 Reversible solid-oxide cells for clean and sustainable energy *Clean Energy* **3** 175–201
[41] Utz A, Hansen K V, Norrman K, Ivers-Tiffée E and Mogensen M 2011 Impurity features in Ni-YSZ-H_2-H_2O electrodes *Solid State Ion.* **183** 60–70
[42] Njodzefon J-C 2015 *Electrode Kinetics and Gas Conversion in Solid Oxide Cells* (Department of Energy Conversion and Storage, Technical University of Denmark)
[43] Utz A, Störmer H, Leonide A, Weber A and Ivers-Tiffée E 2010 Degradation and relaxation effects of Ni patterned anodes in H_2–H_2O atmosphere *J. Electrochem. Soc.* **157** B920
[44] Peksen M 2011 A coupled 3D thermofluid–thermomechanical analysis of a planar type production scale SOFC stack *Int. J. Hydrog. Energy* **36** 11914–28
[45] Tseronis K, Kookos I K and Theodoropoulos C 2008 Modelling mass transport in solid oxide fuel cell anodes: a case for a multidimensional dusty gas-based model *Chem. Eng. Sci.* **63** 5626–38
[46] Vural Y, Ma L, Ingham D B and Pourkashanian M 2010 Comparison of the multicomponent mass transfer models for the prediction of the concentration overpotential for solid oxide fuel cell anodes *J. Power Sources* **195** 4893–904
[47] Fu Y, Jiang Y, Poizeau S, Dutta A, Mohanram A, Pietras J D and Bazant M Z 2015 Multicomponent gas diffusion in porous electrodes *J. Electrochem. Soc.* **162** F613
[48] Rizvandi O B, Miao X-Y and Frandsen H L 2021 Multiscale modeling of degradation of full solid oxide fuel cell stacks *Int. J. Hydrog. Energy* **46** 27709–30
[49] Mogensen M B and Mogensen G 2023 On degradation mechanisms of Ni-YSZ fuel electrodes in solid oxide cells *ECS Trans.* **112** 71–80